On the behavior of high order one-step monotonicity-preserving scheme for direct numerical simulation of turbulent flows

Ismaïl Ben Hassan Saïdi, Guillaume Fournier, Christian Tenaud

On the behavior of high order one-step monotonicity-preserving scheme for direct numerical simulation of shocked turbulent flows.

I. Ben Hassan Saïdi [a] G. Fournier [b] C. Tenaud [a]

[a] *LIMSI, CNRS, Université Paris-Saclay, Orsay, FRANCE.*

[b] *LMEE, Univ. Evry-Val-d'Essonne, Université Paris-Saclay, EVRY, FRANCE*

Abstract

High Reynolds number supersonic flows require accurate predictions, in the one hand, for the design of industrial devices, and on the other hand, for the physical understanding and modeling of these high speed flows that still raise numerous scientific issues. To this end, Direct Numerical Simulations (DNS) are nowadays an adequate tool since all characteristic time and space scales are computed without using any modeling. Among the great variety of high-order numerical schemes using shock-capture features developed for DNS, high-order One-Step (OS) Monotonicity-Preserving (MP) schemes have been developed [1,2] that control the total truncation error involving both errors due to time integration and spatial discretization. The objective of this paper is to check the ability of the high-order OSMP scheme to accurately compute turbulent compressible flows with a special focus on the effect of the MP constraints on solutions of wall bounded turbulent shocked flows. Two canonical test cases are first performed to check separately the ability of the scheme to accurately compute turbulent and shocked flows: *(i)* the classical 3-D Taylor-Green vortex test case [3] is used for evaluating the accuracy of the solver to compute continuous turbulent solutions; *(ii)* the steady 2D shock-wave laminar boundary layer interaction is used for evaluating the shock capturing procedure of the solver. The OSMP scheme is then used to compute an emblematic case of wall bounded turbulent shocked flow where a shock wave interacts with a turbulent boundary layer. A compressible version of the Synthetic Eddy Method is developed for prescribing inflow conditions. We showed that these specific conditions greatly lower the adaptation length compared to more classical inflow conditions. As diffusion in the near wall region is one of the key phenomena, the influence of the viscous flux discretization is reviewed with 2^{nd}-order and 4^{th}-order centered approximations. Compared to reference solutions from the literature, we showed that the OSMP scheme produces reliable solutions that are in very good agreements with references from literature. Even for bounded flows, the use of an order of accuracy higher than the 2^{nd}-order for approximating the diffusive fluxes was shown to have

a negligible influence on solutions. We conclude that the OSMP scheme coupled with a centered 2^{nd}-order approximation for the diffusive fluxes constitutes a reliable numerical tool for the DNS of compressible turbulent shocked flows, that is completely competitive compared to other approaches since the overall errors are lowered of about one order of magnitude for the same grid resolution.

Key words: High-order scheme, shock-capturing feature, compressible flow, Taylor-Green vortex, Turbulent boundary layer, Shock-Wave Boundary Layer Interaction.

---

1 Introduction

High Reynolds number supersonic flows are involved in many applications of industrial fields such as chemical, energy, aeronautical and space industries. In particular in such high speed flows, discontinuities (as shock waves or contact discontinuities), shear layer, turbulence and their interactions occur. They require accurate predictions, mainly in the design of industrial devices since these phenomena can greatly affect their operation and the subsequent aerodynamics loads. Moreover, the physical understanding and modeling of these high speed flows still raise numerous scientific issues. As an example, we can cite shock wave boundary layer interactions (SWBLI) that can possibly occur in flows around supersonic aircrafts, in turbojets, in supersonic air intakes or in rocket nozzles. The dynamics features of such flows are still not fully understood and remains an active field of research. Indeed, SWBLIs are subjected to low frequency longitudinal oscillations called "the unsteadiness" of the SWBLI. The SWBLI unsteadiness stresses solid structures to oscillating loads that can lead to damages of these structures, and therefore needs a very careful attention. Nevertheless, even if this phenomenon is well known, the related physical mechanisms are still debated within the scientific community ([4,5]). Addressing such issues requires fine physical analysis. To this end, the Direct Numerical Simulation (DNS) is a powerful tool since all the scales of the different quantities are computed in the simulation without using any modeling (turbulence modeling, for instance).

DNS of such high Reynolds number compressible flows involving shock waves is a challenging task. High Reynolds number flows are often turbulent and therefore one must use a numerical scheme that represents small scale turbulent structures with the minimum of numerical dissipation. For this purpose, high order schemes are often used, because of "*their potential in delivering higher accuracy with lower cost than low order methods*" as stressed in Wang et al.[3]. Nevertheless, high order schemes are known to produce spurious oscillations in the vicinity of stiff discontinuities such as shock waves (known as the Gibb's phenomenon). On the opposite of a Fully Resolved Simulation (FRS)

approach [6], limited to weak discontinuities where all the scales (including the internal solution of the shock-wave) are resolved, one must then follow a DNS approach where a shock capturing procedure is used to avoid these spurious oscillations. Shock capturing procedures consist in adding artificial diffusion more or less explicitly in the vicinity of discontinuities. They must be restricted to regions near discontinuities without spoiling the accurate predictions away from discontinuities in smooth regions. Mainly, the procedure must be robust enough to maintain the accuracy of the scheme near extrema of the solution.

A review of the high order schemes and shock capturing procedures used for the simulation of turbulent compressibles flows has been performed in [7]. A classical approach consists in the method-of-lines where time and space discretizations are considered separately. Time integration of the semi-discrete form of the Navier-Stokes equations is generally handled by a multistage time integration such as the Runge-Kutta time integration for instance. At each stage of the time integration, high order spatial schemes, equipped with a shock capturing feature for the convective terms that ensures non-oscillatory and conservation properties, are applied for the discretization of the spatial operators (convection and diffusion) of the compressible Navier-Stokes equations. Among the different alternatives, high order Finite Difference (FD) or Finite Volume schemes are frequently used, especially in the academic community for DNS and Large Eddy Simulation (LES) of compressible turbulent flows such as shock wave tubulent boundary layer interactions ([8,9,10,11,12]). Due to their non-dissipative properties, central schemes are often privileged. Nevertheless, these schemes are known to produce numerical instabilities and must be coupled with stabilization methods. The Method-of-lines bears two major drawbacks. The support of high order spatial discretization being relatively wide, applying it in each stage of the time integration leads to very large stencils and hence to high computational efforts and costs. Another drawback of the Runge-Kutta integrations comes from the difficulty to recover Total Variation Diminishing (TVD) properties, to control the development of spurious oscillations, with time integrations greater than the 4th order of accuracy because solving adjoint problems are required that makes resolution much more cumbersome and prohibitively expensive.

Alternatively, following the Lax-Wendroff approach leads to coupled time and space integrations. In this framework, high-order One-Step (OS) schemes have been developed [1,2,13] that control the total truncation error involving both errors due to time integration and spatial discretization. As the integration is only performed in a single step, one of the main advantage of the OS approach is that the global stencil of the scheme is much more *compact* than integration supports used in the method-of-lines for the same order of accuracy. This makes the OS scheme much more competitive in terms of CPU time and memory space consumption. However, solving multi-D equations is much more

delicate since it requires solving a Cauchy-Kovalevskaïa problem [14] that is a complex problem expensive to solve. Alternatives have been proposed to overcome this drawback, and a simplest way to deal with directional operator splitting that is generally retained is the Strang procedure [15,16,17,2]. This procedure allows to recover the good properties of the high order 1D scheme although the overall integration error is dominated by the permutation error of the operators, which is generally of low amplitude.

Whatever the approach used, the high order numerical scheme needs a shock capturing procedure to avoid spurious oscillations arising from the high order discretization near discontinuities. Different shock capturing procedures have been introduced in the literature. The Total Variation Diminishing (TVD) constraints ([18]) are efficient in computing shock waves. Nevertheless, they are known to affect the accuracy of the scheme also in smooth regions of the flow as the TVD constraints are responsible for the so-called clipping of extrema. A way of circumventing this drawback has been introduced by Suresh and Huynh in [19] and further adapted by Daru and Tenaud in [2]. Authors enforced the Monotonicity Preserving (MP) constraints at the discrete level by enlarging the admissible TVD intervals at extrema. The high order flux reconstruction is then preserved everywhere in smooth regions of the flow except near discontinuities where TVD constraints act to avoid spurious oscillations.

Another family of classical shock capturing procedure includes the Essentially Non-Oscillatory (ENO) introduced in [14], and Weighted Essentially Non-Oscillatory (WENO) schemes developed in [20]. These approaches were developed to avoid the spurious oscillations near discontinuities while maintaining high order discretization in smooth regions of the flow (mainly near extrema). Nevertheless, these approach are costly since the flux reconstruction at cell interface must be computed from different competing stencils. Another drawback of the ENO approach is the use of an adaptive stencil that can be the source of numerical artefacts in the results. WENO schemes have been developed to overcome this disadvantage [20] while increasing the accuracy of the approximation by using all possible stencils in the regular region of the solution. Numerical experiments showed [21] that, depending on the Runge-Kutta time integration, the semi-discrete approach based on a high-order WENO scheme can however give oscillatory solutions. Hence, Monotonicity Preserving constraints must be added (named MP-WENO scheme, see Balsara and Shu [21]) to recover a greater stability of this approach.

This explains why, in the context of turbulent shocked flows, a high order One-Step Monotonicity-Preserving (OSMP) scheme [2] has been developed by following a Lax-Wendroff approach. For discontinuity capturing, Monotonicity-Preserving (MP) conditions have been derived to locally relax the TVD constraints in the vicinity of extrema. It was already demonstrated on various

classical 2D test-cases [2,22,23] that this scheme gives very accurate results (in particular, the MP constraint is efficient in canceling the spurious oscillations near discontinuities) at a very low-cost in terms of CPU time since it uses one-step integration, and is therefore very competitive compared to classical high-order method-of-lines coupled with ENO/WENO shock capturing procedures, for instance.

The objective of this paper is to check the ability of the high-order OSMP scheme to accurately compute wall bounded turbulent shocked flows. Two canonical test cases are first performed to check separately the ability of the scheme to accurately compute turbulent and shocked flows: *(i)* the classical 3-D Taylor-Green vortex test case and *(ii)* the steady 2D shock wave laminar boundary layer interaction (SWLBLI). The classical 3-D Taylor-Green vortex test case ([3]) that allows to simulate a turbulent energy cascade in the framework of isotropic homogeneous turbulence, is used for evaluating the accuracy of the solver to compute continuous turbulent solutions. In particular, as far as it acts in regions with extrema, the effect of the MP constraints on solutions of turbulent flows without shock wave is evaluated to study the influence of the shock capturing procedure in "*smooth*" regions. The steady 2D shock-wave laminar boundary layer interaction is used for evaluating the shock capturing procedure of the solver. The influence of the accuracy order of the viscous flux approximation, between the 2^{nd}-order and the 4^{th}-order centered schemes, has also been reviewed on these test cases. The OSMP scheme is then used to compute a shock wave turbulent boundary layer interaction, which is an emblematic case of wall bounded turbulent shocked flow. A Synthetic Eddy Method (SEM) [24,25] that we adapted to compressible flows is employed at the inlet of the domain in order to lower the computational costs associated to the simulation of turbulent boundary layer. This method is extensively presented in appendix A where the simulation of a compressible turbulent boundary layer is presented. The influence of the order of accuracy of the viscous flux discretization is also studied in this context where the diffusion phenomenon are dominant in the near wall region.

The paper is then organized as follows: in section 2, we first recall the governing equations relevant for the simulation of compressible flows, namely the dimensionless form of the compressible Navier-Stokes equations for an ideal gas considered as a newtonian fluid. We then describe the numerical approaches used for discretizing the governing equations in section 3. The OSMP approach is described for computing the non linear advection terms. Regarding the viscous flux approximations, 2^{nd} or 4^{th}-order centered approximations are employed. The simulation of the 3D Taylor-Green Vortex is presented in section 4, and the results are discussed compared to reference solutions. The section 5 is devoted to the simulation of the 2D steady Shock-Wave Laminar Boundary Layer Interaction (SWLBLI) and its comparison with reference solutions. The section 6 is dedicated to the simulation of a Shock-Wave Turbulent Boundary

Layer Interaction (SWTBLI). Both mean properties and dynamical features of the flow are presented. The turbulent inflow implemented in order to lower the numerical costs associated to this simulation (Synthetic Eddy Method) is presented in appendix A. We then conclude on the contributions of this work and address some prospects in the last section.

2 The governing equations

We consider here the dimensionless compressible Navier-Stokes equations expressed in a cartesian coordinate system:

$$\frac{\partial \mathbf{U}}{\partial t} + \nabla \cdot \mathbf{F}(\mathbf{U}) - \nabla \cdot \mathbf{F_v}(\mathbf{U}, \nabla \mathbf{U}) = 0, \tag{1}$$

where $\mathbf{U}$ is the vector of conservative variables, $\mathbf{F}(\mathbf{U})$ the convective fluxes, and $\mathbf{F_v}(\mathbf{U}, \nabla(\mathbf{U}))$ the diffusive fluxes that write respectively:

$$\begin{aligned} \mathbf{U} = \begin{bmatrix} \rho \\ \rho \mathbf{u} \\ \rho E \end{bmatrix}, \quad \mathbf{F} = \begin{bmatrix} \rho \mathbf{u} \\ \rho \mathbf{u} \otimes \mathbf{u} + P\mathbb{I} \\ (\rho E + P)\mathbf{u} \end{bmatrix}, \\ \text{and} \qquad \mathbf{F_v} = \begin{bmatrix} 0 \\ \frac{1}{Re_0}\sigma \\ \frac{1}{Re_0}\mathbf{u}.\sigma + \frac{\mu}{(\gamma-1)Re_0 Pr_0 M_0^2}\nabla T \end{bmatrix}. \end{aligned} \tag{2}$$

$\mathbb{I}$ stands for the identity matrix. ρ is the density, $\mathbf{u}$ is the velocity vector, E is the total energy per unit of mass. P is the thermodynamic pressure related to the conservative variables by the following relationship:

$$P = (\gamma - 1)\left(\rho E - \frac{1}{2}\frac{(\rho \mathbf{u}) \cdot (\rho \mathbf{u})}{\rho}\right),$$

and T is the static temperature expressed following the dimensionless equation of state in the ideal gas assumption:

$$T = \gamma M_0^2 \frac{P}{\rho}. \tag{3}$$

$Re_0 = \dfrac{\rho_0 U_0 L_0}{\mu_0}$ is the Reynolds number, $M_0 = \dfrac{U_0}{c_0}$ is the Mach number, and

$Pr_0 = \dfrac{\mu_0 Cp}{\lambda_0}$ the Prandtl number. $\gamma = \dfrac{Cp}{Cv}$ is the ratio of heat capacities, at constant pression (Cp) and constant volume (Cv).

The viscous stress tensor is expressed as:

$$\sigma = \mu(\nabla \mathbf{u} + \nabla^T \mathbf{u}) - \frac{2}{3}\mu \nabla \cdot \mathbf{u}.$$

We assume that the dynamic viscosity only depends on the temperature through the Sutherland's law. The thermal conductivity is then deduced from the dynamic viscosity once the Prandtl number (Pr_0) is prescribed: $\lambda = \dfrac{\mu Cp}{Pr_0}$.

The reference quantities (noted with a subscript $_0$) are chosen so as to represent the flow characteristics: L_0 is the reference length (m), ρ_0 is the reference density (kg.m^{-3}), U_0 the reference velocity (m.s^{-1}), c_0 is the speed of sound. Specific values of the reference variables will be given in the followings for each test case.

Finally, for a given fluid, *i.e.* for a given value of heat capacity ratio γ, the problem is completely defined as far as 3 dimensionless numbers are prescribed, namely, the Reynolds number (Re_0), the Mach number (M_0) and the Prandtl number (Pr_0).

3 Numerical approaches

The Navier-Stokes equations (1, 2, 3) have been solved using a high order finite volume approach on cartesian meshes. We denote by $\mathbf{U}^n_{i,j,k}$ the discrete quantity $\mathbf{U}(\mathbf{x}, t)$ estimated at a grid point $\mathbf{x}_{i,j,k} = (i\ \delta x, j\ \delta y, k\ \delta z)^{\mathrm{T}}$ and at a time $t^{(n)} = n\ \delta t$ (δt, δx, δy and δz are respectively the time step and the grid spacing in each direction).

An operator splitting procedure is employed that splits the resolution into the Euler part and the viscous problem. The Euler part is discretized by means of a high-order one-step Monotonicity Preserving scheme, namely the OSMPp scheme [2], based on a Lax-Wendroff approach, which ensures a p^{th}-order accuracy in both time and space in the regular regions. Besides, the discretization of the diffusive fluxes is obtained by means of a classical centered (2^{nd}-order or 4^{th}-order) scheme that has been coupled to a 2^{nd}-order Runge-Kutta time integration.

3.1 The One-Step Monotonicity-Preserving (OSMP) scheme.

3.1.1 The unlimited OS scheme.

We first present the unlimited scheme on the one dimensional Euler equation:

$$\frac{\partial \mathbf{U}}{\partial t} + \frac{\partial \mathbf{F}(\mathbf{U})}{\partial x} = \mathbf{0}. \tag{4}$$

This equation is discretized using the following conservative approximation:

$$\mathbf{U}_i^{n+1} = \mathbf{U}_i^n - \frac{\delta t}{\delta x}(\mathbf{F}_{i+1/2} - \mathbf{F}_{i-1/2}). \tag{5}$$

The numerical flux $F_{i+1/2}$ is approximated by a p^{th}-order One-Step scheme (OSp) developed in [2] :

$$\mathbf{F}_{i+1/2} = \mathbf{F}^{Roe}_{i+1/2} + \frac{1}{2}\sum_k \left(\Phi^p_k(1-|\nu_k|)\,\delta\alpha_k\,|\lambda_k|\,.\mathbf{r}_k\right)_{i+1/2}, \tag{6}$$

where $\mathbf{F}^{Roe}_{i+1/2}$ is the Roe flux at the cell interface:

$$\mathbf{F}^{Roe}_{i+1/2} = \frac{1}{2}\left(\mathbf{F}(\mathbf{U}_i^n) + \mathbf{F}(\mathbf{U}_{i+1}^n)\right) - \frac{1}{2}\sum_k \left(|\lambda_k|\,\delta\alpha_k.\mathbf{r}_k\right)_{i+1/2}.$$

$\delta\alpha_{ki+1/2} = \mathbf{l}_{ki+1/2}\cdot\left(w^n_{i+1} - w^n_i\right)$ is the k^{th} Riemann invariant. $\lambda_{ki+1/2}$, $\mathbf{l}_{ki+1/2}$, and $\mathbf{r}_{ki+1/2}$ are respectively the k^{th} eigenvalue, and the corresponding left and right eigenvectors of the Jacobian matrix of the Euler flux ($\nabla_{\mathbf{U}}\mathbf{F}(\mathbf{U})$), expressed at the cell interface. $\nu_{ki+1/2} = \dfrac{\delta t}{\delta x}\lambda_{ki+1/2}$ is the local CFL number evaluated at cell interfaces.

Since in the One Step procedure the even derivatives are expressed using centered approximations while the odd ones use upwind approximations, the p^{th}-order accuracy functions ($\Phi^{\,p}_{k\,i+1/2}$) are split into even and odd contributions following:

$$\Phi^{\,p}_{k\,i+1/2} = \sum_{n=1}^{m} \Psi^{\,2n}_{k\,i+1/2} - js\sum_{n=1}^{m_1} \Psi^{\,2n+1}_{k\,i+1/2-js/2}, \tag{7}$$

where $m = \lfloor p/2 \rfloor$, $m_1 = \lfloor \dfrac{(p-1)}{2} \rfloor$ ($\lfloor\ \rfloor$ is the integer division symbol), and $js = sign(\lambda_{ki+1/2})$. The even and odd functions $\Psi^{\,2n}_{k\,i+1/2}$ and $\Psi^{\,2n+1}_{k\,i+1/2-js/2}$ are given by the recurrence formula (for $n \geq 1$):

$$\Psi^{\,2n}_{k\,i+1/2} = \sum_{l=0}^{2n-2} (-1)^l C^l_{2n-2}.(c_k{}^{(2n)}\delta\alpha_k)_{i+1/2+n-1-l}, \tag{8}$$

$$\Psi^{\,2n+1}_{k\,i+1/2} = \sum_{l=0}^{2n-1} (-1)^l C^l_{2n-1}.(c_k{}^{(2n+1)}\delta\alpha_k)_{i+1/2+(n-1-l).js}; \tag{9}$$

where $C_r^l = \dfrac{r!}{(r-s)!s!}$.

The coefficients ${c_k}^{(q)}$ depend on the local CFL number ($\nu_{ki+1/2}$), and are given by:

$$({c_k}^{(q+1)})_{i+1/2} = \frac{|\nu_k|_{i+1/2} + (-1)^q \lfloor \frac{(q+1)}{2} \rfloor}{q+1} . ({c_k}^{(q)})_{i+1/2}, \quad q \geqslant 2. \tag{10}$$

with

$$c_k{}^2_{i+1/2} = |\lambda_k|_{i+1/2} (1 - |\nu_k|_{i+1/2}) \tag{11}$$

Using the accuracy function Φ^p (7), the scheme is p^{th}-order accurate in both space and time. This scheme has been derived up to the 11th-order and more detailed information can be found in Daru & Tenaud [2] and Daru & Gloerfelt [26]. In the following, accuracy functions of 5^{th}-order and 7^{th}-order have been used for computing test-case solutions.

3.1.2 The limited OSMP scheme.

In a classic way for high order approximations, spurious oscillations could occur in the vicinity of discontinuities. Total Variation Diminishing (TVD) constraints are commonly employed to cure this problem. Nevertheless, as it is well known, the TVD constraints clip the extrema although the solution is smooth [2]. To overcome this drawback, we employ Monotonicity-Preserving (MP) constraints that locally relax the TVD constraints near extrema. These constraints, first developed by Suresh and Huynh [19] and further extended by Daru and Tenaud [2], are applied on the accuracy function (Φ^{p-MP}) to recover a scheme that is p^{th}-order in time and space everywhere except near discontinuities where the scheme is Monotonicity-Preserving [2].

3.1.3 Extension to 3D systems of equations.

The extension in the multidimensional case is delicate as far as a coupled time and space approach is used. In fact, we need to consider cross derivative terms that appear in the second and higher order terms, which are left uncontrolled if one applies a direction by direction MP correction to a Lax-Wendroff unsplit scheme. We also need to guarantee that the resulting scheme is non-oscillatory. The simplest way to avoid solving a Cauchy-Kovalevskïa problem to account for cross derivatives and to recover good properties of the one-dimensional scheme is to use a Strang directional splitting strategy [15,16,17,2] which is unfortunately only second order accurate when directional operators do not commute. However, this error is of low amplitude since it is only related to the permutation error when operators do not commute. While the order of accuracy is lowered compared to the tensorial multistage approach, the OSMP

scheme with the Strang algorithm provides results with very small error level at low cost [2,22].

In three dimensions, the splitting of the system of equations can be constructed to give symmetric accurate solution every six time steps:

$$\begin{aligned}\mathbf{U}_{i,j,k}^{n+6} = & \left(L_{\delta x}(\delta t)\cdot L_{\delta y}(\delta t)\cdot L_{\delta z}(\delta t)\right)\left(L_{\delta x}(\delta t)\cdot L_{\delta z}(\delta t)\cdot L_{\delta y}(\delta t)\right)\\ & \left(L_{\delta y}(\delta t)\cdot L_{\delta z}(\delta t)\cdot L_{\delta x}(\delta t)\right)\left(L_{\delta y}(\delta t)\cdot L_{\delta x}(\delta t)\cdot L_{\delta z}(\delta t)\right)\\ & \left(L_{\delta z}(\delta t)\cdot L_{\delta y}(\delta t)\cdot L_{\delta x}(\delta t)\right)\left(L_{\delta z}(\delta t)\cdot L_{\delta x}(\delta t)\cdot L_{\delta y}(\delta t)\right)\cdot \mathbf{U}_{i,j,k}^{n}.\end{aligned}$$

Here $L_{\delta x}$, $L_{\delta y}$ and $L_{\delta z}$ are discrete approximations of the Euler operators in each space direction. For instance, $L_{\delta x}$ denotes the Euler operator of the following problem:

$$L_{\delta x}(\delta t)\left(\mathbf{U}_{i,j,k}^{m}\right) = \mathbf{U}_{i,j,k}^{m} - \frac{\delta t}{\delta x}\left(\mathbf{F}_{i+1/2}^{m} - \mathbf{F}_{i-1/2}^{m}\right)_{j,k}$$

3.2 Approximation of the viscous fluxes.

The temporal discretization of the diffusive fluxes is obtained by means of a 2^{nd}-order Runge-Kutta time integration. In each sub step of the Runge-Kutta integration, a classical central finite difference scheme is applied to approximate the divergence of the viscous fluxes. To study the influence of the order of accuracy of the viscous fluxes especially in case of wall bounded flows, two spatial approximations have here been checked: a 2^{nd}-order accurate centered scheme and a 4^{th}-order centered scheme.

3.2.1 2^{nd}-order approximation:

Considering the direction (ξ) normal to the cell interface, we look for a numerical approximation of the viscous flux $\mathbf{F}_{\mathbf{v}}^{\xi}(\mathbf{U}, \nabla\mathbf{U})$ at the cell interface $(i+1/2)$ that satisfies the relationship:

$$\frac{\partial \mathbf{F}_{\mathbf{v}}^{\xi}}{\partial \xi}\,|_{i,j,k} = \frac{1}{\delta\xi}\left(\mathbf{F}_{\mathbf{v}i+1/2} - \mathbf{F}_{\mathbf{v}i-1/2}\right)_{j,k} + O(\delta\xi^2).$$

This is fulfilled once the velocity and temperature gradients involved in the numerical viscous fluxes satisfy the following relationships:

- in the normal to the cell interface (ξ), considering the cell centered variable ϕ, the gradient at the cell interface is:

$$\frac{\partial \phi}{\partial \xi}\Big|_{i+1/2,j,k} = \frac{1}{\delta\xi}\left(\phi_{i+1,j,k} - \phi_{i,j,k}\right) + O(\delta\xi^2);$$

- in tangential directions (represented by η), lying in the plane of the cell interface, the gradient is expressed as:

$$\frac{\partial \phi}{\partial \eta}\Big|_{i+1/2,j,k} = \frac{1}{4.\delta\eta}\left(\phi_{i+1,j+1,k} + \phi_{i,j+1,k} - \phi_{i+1,j-1,k} - \phi_{i,j-1,k}\right) + O(\delta\eta^2).$$

3.2.2 4^{th}-order approximation:

Considering the direction (ξ) normal to the cell interface, we look for a numerical approximation of the viscous flux $\mathbf{F}_{\mathbf{v}}^{\xi}(\mathbf{U}, \nabla\mathbf{U})$ at the cell interface $(i+1/2)$ that satisfies the relationship:

$$\frac{\partial \mathbf{F}_{\mathbf{v}}^{\xi}}{\partial \xi}|_{i,j,k} = \frac{1}{\delta\xi}\left(\mathbf{F}_{\mathbf{v}i+1/2} - \mathbf{F}_{\mathbf{v}i-1/2}\right)_{j,k} + O(\delta\xi^4).$$

This is fulfilled once the velocity and temperature gradients involved in the numerical viscous fluxes satisfy the following relationships:

- in the normal to the cell interface (ξ), considering the cell centered variable ϕ, the gradient at the cell interface is:

$$\frac{\partial \phi}{\partial \xi}\Big|_{i+1/2,j,k} = \frac{1}{12.\delta\xi}\left(\phi_{i-1,j,k} - 15.\phi_{i,j,k} + 15.\phi_{i+1,j,k} - \phi_{i+2,j,k}\right) + O(\delta\xi^4);$$

- in tangential directions (represented by η), lying in the plane of the cell interface, the gradient is expressed as:

$$\frac{\partial \phi}{\partial \eta}\Big|_{i+1/2,j,k} = \frac{1}{12.\delta\eta}\left(\widehat{\phi}_{i+1/2,j-2,k} - 8.\widehat{\phi}_{i+1/2,j-1,k} + 8.\widehat{\phi}_{i+1/2,j+1,k} - \widehat{\phi}_{i+1/2,j+2,k}\right) + O(\delta\eta^4),$$

with

$$\widehat{\phi}_{i+1/2,j,k} = \frac{1}{12.}\left(-\phi_{i-1,j,k} + 7.\phi_{i,j,k} + 7.\phi_{i+1,j,k} - \phi_{i+1,j,k}\right).$$

3.2.3 Check of the order of accuracy on a manufactured solution.

The approximation of the viscous fluxes introduced above has been validated using a manufactured solution corresponding to the initial flow field of the well known three-dimensional Taylor-Green vortex test case (see the section § 4 for the initial state). The following 3-D diffusive problem has been solved with an initial flow field at rest:

$$\frac{\partial \mathbf{U}}{\partial t} - \nabla \cdot \mathbf{F}_{\mathbf{v}}\left(\mathbf{U}, \nabla\mathbf{U}\right) = \mathbf{S}\left(\mathbf{U}, \nabla\mathbf{U}\right), \tag{12}$$

where $\mathbf{S}\left(\mathbf{U}, \nabla\mathbf{U}\right)$ is the source term equal to the viscous flux computed analytically from the reference flow field of the Taylor-Green vortex test case.

The solution of equation (12) converges towards the initial flow field of the Taylor-Green vortex test case with a zero machine residual. Figure 1 shows the L_2 norm of the error on the longitudinal velocity component between the reference Taylor-Green vortex solution (*i.e.* the initial state) and the steady solution obtained with the 2^{nd}- or the 4^{th}-order approximations of the viscous fluxes. These errors are plotted versus the grid spacing $h = \dfrac{1}{N}$ (N being the number of equally spaced grid points in each direction).

We clearly observe that the theoretical order of accuracies (*i.e.* 2^{nd} and 4^{th} orders) are clearly retrieved with however a slight over-convergence observed. These results clearly validate the implementation of the 2^{nd}- and 4^{th}-order approximations of the viscous fluxes.

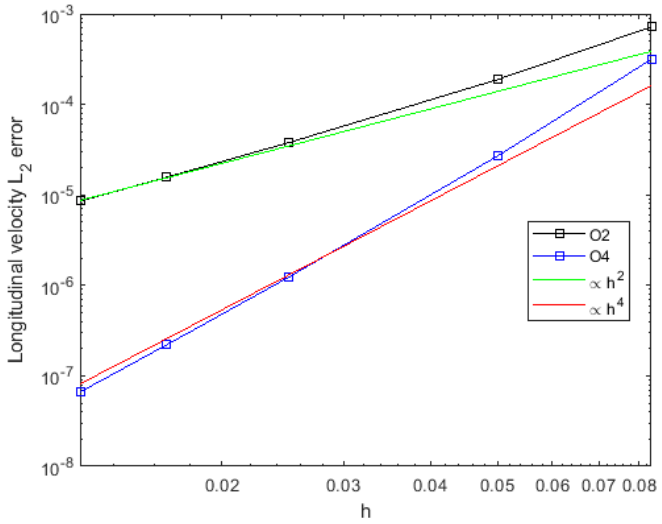

Fig. 1. The L_2 norm of errors on the longitudinal velocity component, versus the grid spacing, of the Taylor Green vortex between the reference and the computed solution using either the 2^{nd}-order or the 4^{th}-order approximations of the viscous fluxes.

Equivalent results were also obtained for the other components of the velocity.

4 Direct numerical Simulation of the 3D Taylor-Green vortex

First, the well documented 3-D Taylor-Green vortex is considered at a Reynolds number of $Re = 1600$ [27,3]. The Taylor-Green vortex is a simple configuration allowing to simulate a turbulent energy cascade with charateristics very close to those of the Isotropic Homogeneous Turbulence (IHT). This problem allows us to evaluate the ability of the numerical procedure to compute transitional solutions in decaying IHT.

A 3D periodic domain (Ω) of 2π non-dimensional side length is considered, in which a non dimensional initial flow field, which is an analytic solution of the Navier-Stokes equations, is given. This initial flow field, consisting in eight planar vortices, writes:

$$\begin{aligned}
u &= sin(x)cos(y)cos(z), \\
v &= -cos(x)sin(y)cos(z), \\
w &= 0, \\
P &= \frac{1}{\gamma M_0} + \frac{1}{16}(cos(2x) + cos(2y))(cos(2z) + 2), \\
T &= 1, \\
\rho &= \frac{\gamma P M_0^2}{T}, \\
E &= \frac{1}{(\gamma - 1)\gamma M_0^2} T + \frac{1}{2}(u^2 + v^2 + w^2).
\end{aligned} \tag{13}$$

Nonlinear interactions between these initial vortices create smaller and smaller vortices until kinetic energy dissipation into heat occurs following the so called Kolmogorov energy cascade.

The flow is completely characterized by the following set of non dimensional values:

$$\begin{aligned}
M_0 &= \frac{U_0}{c_0} = 0.1, \\
\gamma &= 1.4, \\
Re_0 &= \frac{\rho_0 U_0 L_0}{\mu_0} = 1600, \\
Pr_0 &= \frac{\mu_0 Cp_0}{\lambda_0} = 0.71,
\end{aligned} \tag{14}$$

where the reference variables (index 0) refer to the flow at the initial state. U_0 is the greatest value of the flow speed in the domain. c_0 is the speed of sound, given by the uniform initial temperature T_0. $L_0 = 2\pi$ is the characteristic size of the domain. μ_0 and λ_0 are respectively the initial dynamic viscosity and thermal conductivity of the fluid, given by the uniform temperature T_0. As the flow is considered almost incompressible ($M_0 = 0.1$), μ and λ are considered as constant.

Several uniform grids have been used to study grid convergence (namely, 32^3, 64^3, 128^3, 256^3 and 512^3). To judge of the quality and accuracy of the solution, several integral quantities have been computed to be compared to the literature:

- The integral of the kinetic energy over the domain (Ω) is calculated at every

time step during the simulation as follows:

$$E_k = \frac{1}{|\Omega|}\int_\Omega \rho \frac{\mathbf{u}\cdot\mathbf{u}}{2} d\Omega, \tag{15}$$

where $|\Omega|$ is the measure of the domain (Ω).

- The kinetic energy dissipation at every time step is defined as:

$$\epsilon = -\frac{dE_k}{dt}. \tag{16}$$

The kinetic energy dissipation is computed using equation (16) by first order time derivatives of the kinetic energy.

- The enstrophy integral over the domain Ω is given by:

$$\varepsilon = \frac{1}{|\Omega|}\int_\Omega \rho \frac{\boldsymbol{\omega}\cdot\boldsymbol{\omega}}{2} d\Omega, \tag{17}$$

where $\boldsymbol{\omega} = \nabla \times \mathbf{u}$. The vorticity components are calculated from the velocity derivatives approximated by using a 4^{th}-order Pade scheme [28].

The time evolution of the kinetic energy, its dissipation and the enstrophy production in the domain are pivotal quantities representative of both the energy cascade between turbulent scales and the turbulent vorticity production.

4.1 Results using the unlimited OS scheme and the 2^{nd}-order viscous fluxes approximation.

As this flow does not exhibit discontinuity, simulations are first performed using the unlimited OS-7 scheme and a 2^{nd}-order spatial discretization for the diffusive terms. A constant CFL number value of 0.5 is used.

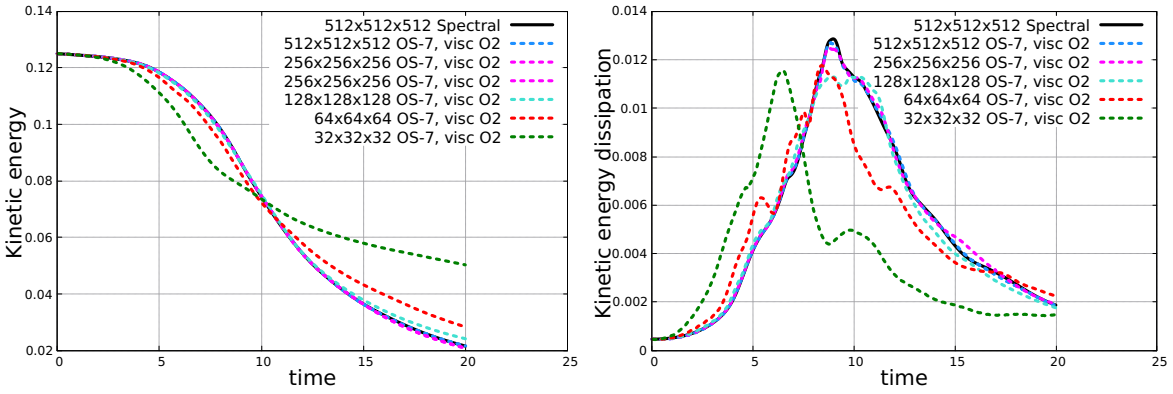

Fig. 2. History of the kinetic energy (on the left) and the kinetic energy dissipation (on the right) obtained using the OS-7 scheme on several mesh sizes (32^3, 64^3, 128^3, 256^3 and 512^3.): present solutions are compared to the reference solution [3].

Figure 2 shows respectively the evolution with time of the kinetic energy (on the left) and its dissipation (on the right) for several mesh sizes (32^3, 64^3, 128^3, 256^3 and 512^3). Results are compared to a reference solution obtained by a de-aliazed pseudo-spectral spatial discretization coupled with a three-step Runge-Kutta scheme for the time integration, on a 512^3 grid [3]. We observe the convergence of the solution toward the reference solution when the mesh is refined. The decrease of the kinetic energy in the domain can be split into two separate zones. In the first zone between times 0 and 9, the kinetic energy dissipation increases until it reaches a maximum value of almost 0.013 around time 9. This growth of kinetic energy dissipation is related to the transition towards turbulence creating smaller and smaller structures through the Kolmogorov energy cascade until the energy dissipation into internal energy occurs. The maximum of kinetic energy dissipation corresponds to an inflection point in the history of the kinetic energy. As far as no energy has been injected into the domain (Ω) from the initial time, this maximum dissipation is followed by a second period where the dissipation decreases as the flow relaxes.

On the one hand, it is clearly visible in figure 2 that simulations on meshes 32^3 and 64^3 completely fail to recover the right behavior since the histories of kinetic energy and kinetic energy dissipation computed on these two meshes largely differ from the reference solution. As meshes are not fine enough to capture small scales, the maximum of the kinetic energy dissipation, acting at small scales, occurs too early.

Simulations on meshes 128^3 and 256^3 exhibit rather good agreement with the reference solution for both the kinetic energy and the dissipation, as shown in figure 2. Results obtained on 256^3 grid points are almost superposed with the reference solution except near $t \simeq 15-16$. Mainly, the values of the maximum of the kinetic energy dissipation and its time location obtained on 256^3 grid points are clearly in accordance with the reference and largely better computed than using 128^3 points. The results obtained on 512^3 grid points are better than the results obtained on the other meshes. It highlights the importance of the mesh refinement on the accuracy of the solution. Results obtained on 512^3 grid points are almost perfectly superposed with the reference solution. It shows that with the same resolution, the OS scheme reaches the same precision than the pseudo spectralcode.

The same simulations have secondly been performed using the 5^{th}-order One Step scheme (OS-5). In order to quantify the grid convergence, we define the L_∞ and L_2-norms error of a quantity s with respect to the reference solution s^{ref} as:

$$Error_{L_\infty(t^k\in[0;10])} = max_{(t^k\in[0;10])} \mid s_k - s_k^{ref} \mid, \tag{18}$$

$$Error_{L_2(t^k\in[0;20])} = \sqrt{\frac{1}{20}\sum_k \mid s_k - s_k^{ref} \mid^2 dt}, \tag{19}$$

where s_k is the value of s at time $t^k = k.\delta t$ (with δt the time step and $k \in \mathbb{N}$), and s_k^{ref} is the reference value (pseudo-spectral spatial discretization on a 512^3 grid [3]) of s at time t^k. The L_∞ norm is computed considering only the first half of the simulation time as it was defined in the 4-th International Workshop on High-Order CFD Methods (HiOCFD4) [29], while the L_2 norm is computed considering the whole simulation time. Linear interpolation is used to evaluate the value of s at the same discrete times t^k as the reference solution s^{ref}. The L_2 and L_∞ error norms on the kinetic energy dissipation are plotted in figure 3 versus the grid spacing $h = \dfrac{1}{N}$ (N is the number of grid points in each direction). Since errors are calculated with respect to an approximated solution (de-aliased pseudo-spectral solution on 512^3 grid), slopes do not correctly reflect on the order of accuracy.

On the L_2 error norms (figure 3-left), the higher the order of accuracy of the One-Step scheme, the lower the error level with respect to the reference solution for the same mesh size. It is then possible to obtain the same error level with a lower order of accuracy if a finer grid is used. For instance, to recover the same error level on the L_2 norm as the one obtained with the 7th-oder One-Step scheme using 32^3 grid points, we need 42^3 grid points with the 5th-order OS scheme. To know if it is relevant to use a higher order scheme, we computed the CPU time of the simulation for each case. The OS-7 scheme on 32^3 grid points needs only 90 % of the CPU time used by the OS-5 scheme on 42^3 grid points. We conclude and claim that the use of the highest order tested of the OS scheme is relevant in term of simulation time and accuracy compromise.

To compare with, best results obtained in the HiOCFD4 workshop [29] using the DG-4 scheme are also plotted on the right part of figure 3, regarding the L_∞ error norms. Results obtained using the OS-5 and OS-7 schemes compare very favorably with one of the best results obtained by the HiOCFD4 workshop participants [29,3] since L_∞ error norms of the OS schemes are more than one order of magnitude smaller than the one obtained using the DG-4 scheme. To recover the same error levels, the DG-4 scheme therefore needs far more points than the OS-7 scheme.

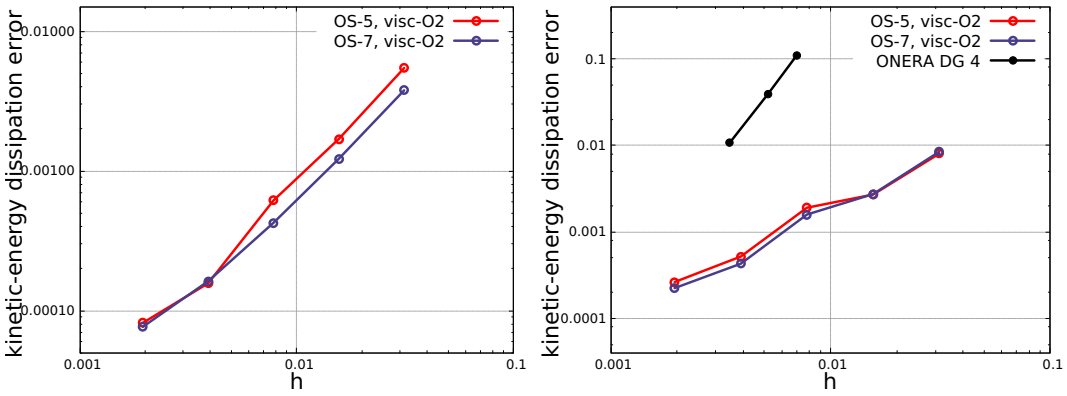

Fig. 3. On the left, L_2 error norms on the kinetic energy dissipation with respect to the reference [3] versus the grid spacing (h). On the right, comparison on the L_∞ error norms between the 5th-order and 7th-order One-Step schemes and the DG-4 scheme [29].

The enstrophy, is then computed by equation (17). The history of the enstrophy production is plotted in figure 4 on the left. As for the kinetic energy dissipation, it is splitted in two different areas. The first region corresponds to the transition towards turbulence; the enstrophy increases until it reaches a maximum value of 10.25 around time equal 9. Then, in the second region, the enstrophy decreases as the flow relaxes. Again, the finer the mesh, the closer to the reference the estimation of the enstrophy production. The time when maximum enstrophy occurs and its maximum value are not well predicted when using the 32^3 and 64^3 meshes. The prediction of the time of maximum enstrophy is correct when 256^3 grid points are used, but its value is slightly underestimated. The enstrophy obtained on 512^3 grid points is almost perfectly superposed with the reference solution. Results obtained with the One-Step approach on the enstrophy production compare well with results of the HiOCFD4 workshop [29,3] as shown in figure 4-right, where the L_∞ entrophy dissipation error with respect to the reference solution is plotted versus the mesh size. The grid convergence is clearly visible in figure 4-right. We see that the higher the order of the OS scheme, the lower the error. The discrepancies between the error obtained with the DG-4 scheme and the OS scheme is not as large as for the kinetic energy dissipation error. The DG-4 scheme still needs however far more points than the OS schemes to recover the same error level on enstrophy dissipation.

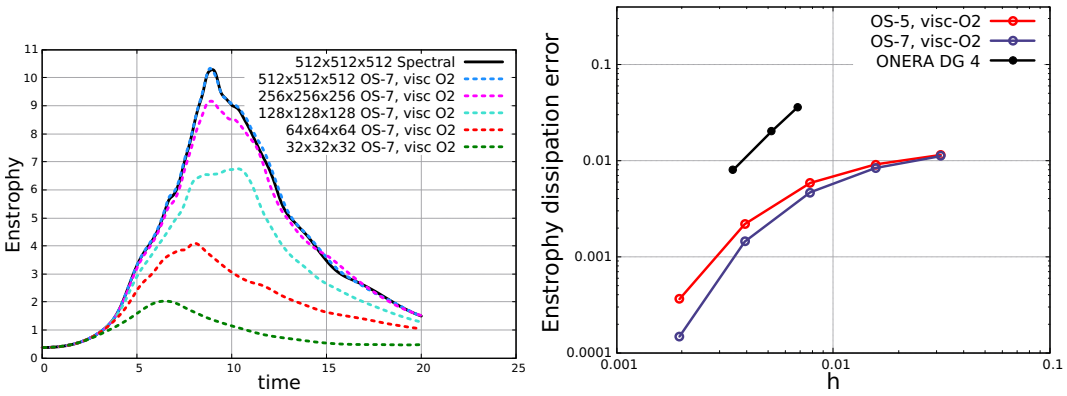

Fig. 4. On the left, history of the enstrophy obtained by using the OS-7 scheme on several mesh sizes (32^3, 64^3, 128^3, 256^3 and 512^3): present solutions are compared to the reference solution [3]. On the right, L_∞ error norms on the kinetic energy dissipation with respect to the reference [3] versus the grid spacing (h): comparison between the 5th-order and 7th-order One-Step schemes and the DG-4 scheme [29].

4.2 Effect of the MP constraint on the results.

The previous simulations have also been performed using the shock capturing procedure to check the influence of the Monotonicity-Preserving constraints on a smooth solution since this procedure, inherently diffusive, could spoil the solution obtained through an accurate scheme.

The comparison between the time evolution of the kinetic energy dissipation computed with the unlimited scheme (OS-7) and with the MP procedure (OSMP-7) on the 256^3 and 512^3 meshes is plotted in figure 5. Results are almost the same with very small discrepancies, visible for the simulation using 256^3 grid points, demonstrating that the MP constraints have a very little influence on a smooth solution. These small discrepancies vanish when the mesh is sufficiently refined with 512^3 grid points.

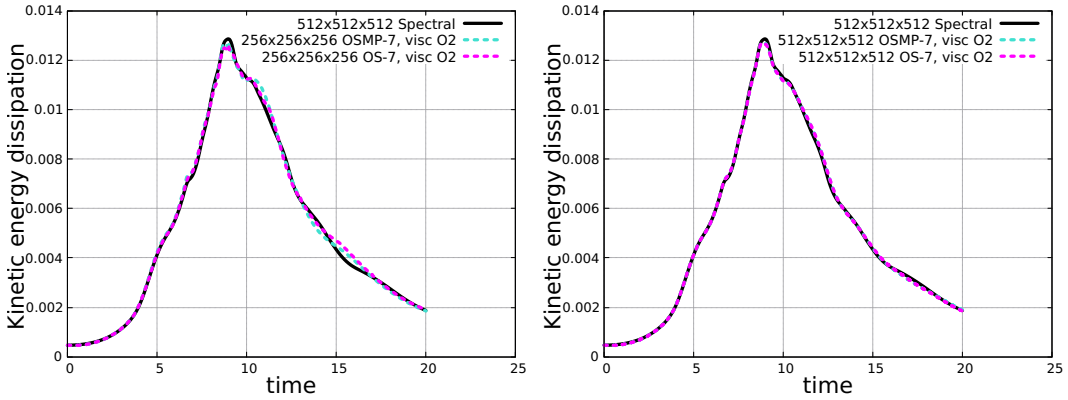

Fig. 5. History of the kinetic energy dissipation obtained with and without a schock–capturing procedure on a meshes with 256^3 and 512^3 grid points. OS-7 and OSMP-7 solutions are compared to the reference solution [3]. On the left: mesh with 256^3 grid points. On the right: mesh with 512^3 grid points.

The comparison between the time evolution of the kinetic energy dissipation computed using only TVD constraint (OSTVD-7) or the MP procedure (OSMP-7) on the 256^3 and 512^3 meshes is plotted in figure 6. The results show that the use of the TVD constraint spoils the smooth solution (clipping of extrema of the solution [2,22]) and the MP procedure efficiently circumvent this drawback. Indeed regarding the TVD results, on the 256^3 mesh, discrepancies between the solutions are visible for $t > 8-9$. Discrepancies are also obtained on the 512^3 mesh for $t > 12-13$.

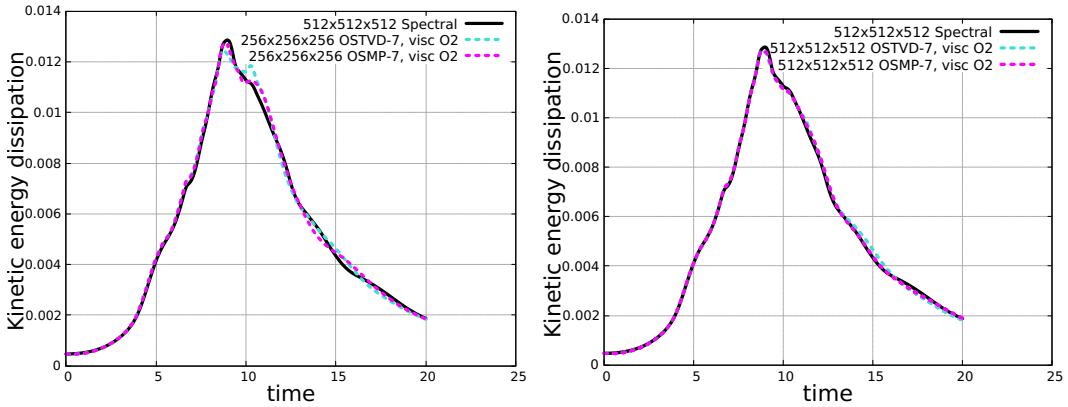

Fig. 6. History of the kinetic energy dissipation. The results obtained using the TVD constraint (OSTVD-7) and the MP constraint (OSMP-7) are compared to the reference solution [3]. On the left: mesh with 256^3 grid points. On the right: mesh with 512^3 grid points.

The L_2 error norms with respect to the reference, obtained with and without the MP procedure are plotted in figure 7 for the kinetic energy dissipation (on the left) and for the enstrophy (on the right). Similar level of errors are

recovered in both cases. The use of the shock capturing procedure has a very weak influence on the computation of the kinetic energy dissipation and on the enstrophy in the domain. These results show that the MP constraint can efficiently be used to simulate regular flows.

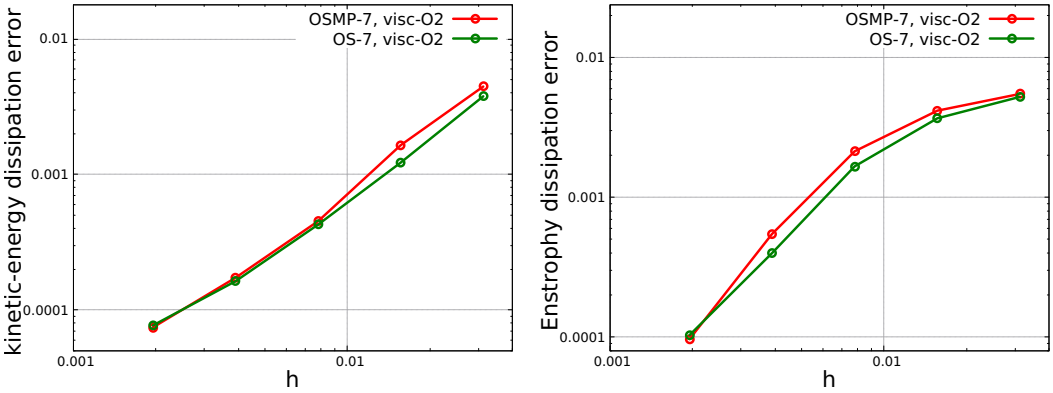

Fig. 7. L_2 error norms with respect to the reference [3] versus the grid spacing (h), on the kinetic energy dissipation (on the left) and on the enstrophy (on the right): comparison between the unlimited (OS-7) and the MP (OSMP-7) 7th-order One-Step schemes.

4.3 Influence of the accuracy order of approximation of the diffusive fluxes.

Simulations have also been performed using a 4^{th} order centered finite difference approximation for the diffusive fluxes as far as the high order approximation might have an influence on the dissipation process occurring at small scales. This scheme is coupled with a OSMP-7 scheme for the advection approximation.

The history of the kinetic energy dissipation obtained with a 4^{th}-order centered viscous fluxes on the 256^3 and 512^3 meshes is compared with the results obtained using a 2^{nd}-order centered finite difference approximation for the diffusive fluxes in figure 8. The use of an order higher than second order for the diffusive fluxes have a negligeable influence on the results for such well resolved simulations at relatively high Reynolds number. Very small discrepancies are only visible for the simulation on the 256^3 mesh in the second part of the distribution where dissipation plays a key role in the turbulence relaxation. These discrepancies are not relevant to justify the use of high-order viscous discretization especially since they completely vanish on the 512^3 mesh.

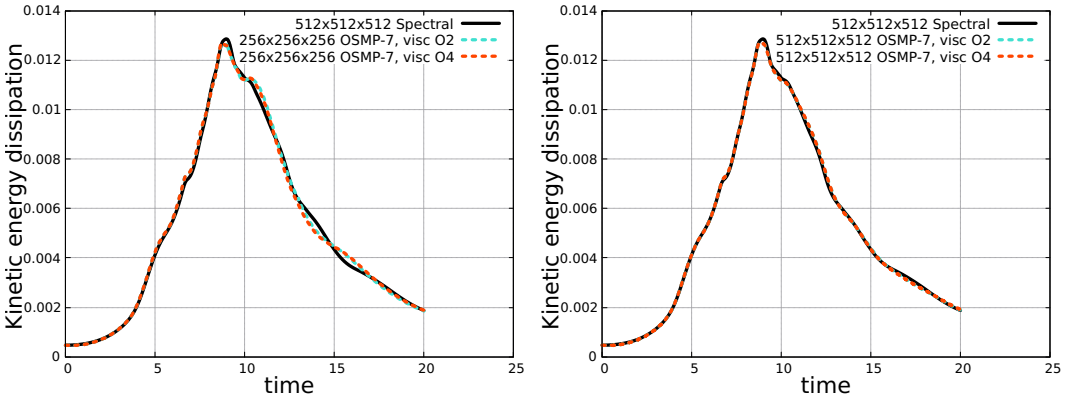

Fig. 8. History of the kinetic energy dissipation obtained using the OSMP-7 on the 256^3 mesh. Comparison between results obtained with a second 2^{nd}-order and a 4^{th}-order discretization for the diffusive fluxes. Present solutions are also compared to the reference solution [3].

The L_2 errors are nearly the same in both cases as shown in figure 9. The use of the 4^{th}-order discretization of the viscous fluxes leads to a drastic increase of the computational time of 65 % with respect to the one of a 2^{nd}-order approximation of the viscous fluxes. These results demonstrate that using approximations of order higher than the 2^{nd}-order for the diffusive fluxes is not relevant for such unbounded high Reynolds number configurations.

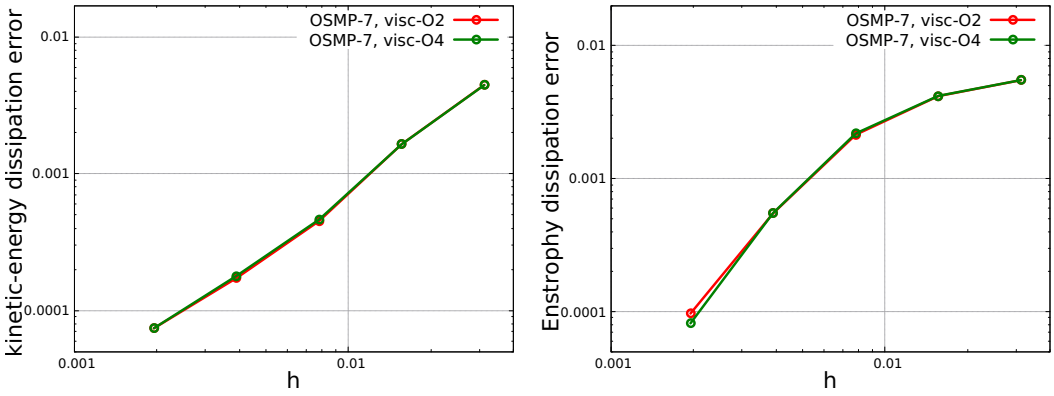

Fig. 9. L_2 error norms with respect to the reference [3] versus the grid spacing (h), on the kinetic energy dissipation (on the left) and on the enstrophy (on the right): comparison between the 2^{nd}-order and the 4^{th}-order approximations of the viscous fluxes.

5 Shock-wave laminar boundary layer interaction.

Secondly, the ability of the present numerical procedure to compute discontinuous solutions have been reviewed. We consider the interaction between

an incident oblique shock wave impinging a laminar boundary layer developing over a flat plate. The interaction produces a separation of the flow and a subsequent recirculation bubble. This flow which here is steady has been experimentally and numerically studied in [30].

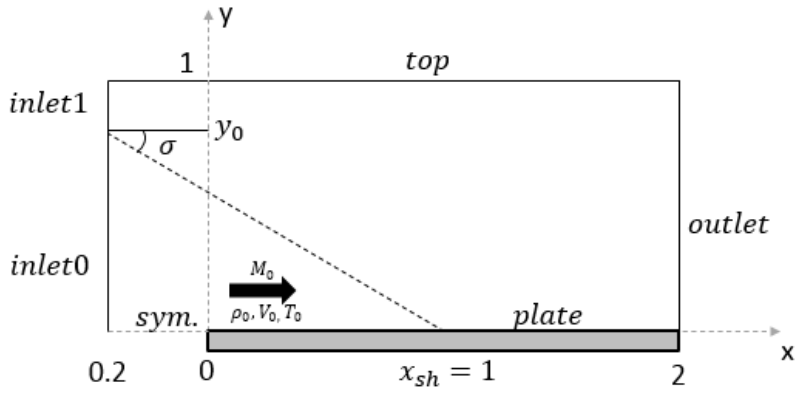

Fig. 10. Sketch of the computational domain for the shock-wave boundary layer interaction: non-dimensional dimensions and boundary conditions. The dashed line represents the inviscid incident shock-wave location [31].

The flow consists in a supersonic uniform flow over a flat plate leading to the development of a laminar boundary layer. Sketch of the computational domain is given in figure 10. A supersonic uniform flow is imposed at the inlet. At a height (y_0), the Rankine-Hugoniot relationships are prescribed, so that a shock-wave at an angle $\sigma = 30.8°$ is created in the domain that impinges the wall at $x_{sh} = 1$ (*i.e.* the length from the leading edge of the plate at which the shock impacts the plate in the non viscous regime is taken as the reference length). No-slip and adiabatic wall conditions are prescribed for $y = 0$ and $x > 0$ whereas a symmetry boundary condition is imposed in front of the leading edge of the flat plate. Outlet time dependent non-reflecting boundary conditions are prescribed at the top and at the outlet boundaries [32] (see Fig. 10).

The flow in the region *inlet 0* ($y < y_0$) is prescribed by using the similitude numbers that completely characterize the flow:

$$\begin{aligned} M_0 &= \frac{U_0}{c_0} = 2.15, \\ Re_0 &= \frac{\rho_0 U_0 x_{sh}}{\mu_0(T_0)} = 10^5, \\ Pr_0 &= \frac{\mu_0 Cp_0}{\lambda_0(T_0)} = 0.71, \\ \gamma &= 1.4, \end{aligned} \tag{20}$$

where subscript 0 denotes values prescribed at the inlet boundary region *inlet 0*. The dynamic viscosity μ_0 and the thermal conductivity λ_0 is given by the Sutherland's law, once the inlet temperature (T_0) prescribed.

The domain is discretized by using a cartesian mesh with non uniform spacing in both x and y directions. In the longitudinal direction, the mesh is refined in the vicinity of the flat plate leading edge and in the vicinity of the shock wave impact abscissa (x_{sh}). In the vertical direction, the mesh is tightened close to the wall using a hyperbolic tangent law to obtain a minimum grid spacing over the plate of $\Delta y_{min} = 10^{-4}$.

The presence of the impinging shock wave imposes a sharp adverse pressure gradient to the boundary layer. As accurately described by Delery in [4], in the configuration presently studied, the adverse pressure gradient is strong enough to initiate a separation of the boundary layer that reattaches further downstream forming a closed separation bubble. This kind of shock wave boundary layer interaction is called strong interaction because of the large separation occurring (on the contrary of a weak interaction without a separation). The flow being subsonic in the wall vicinity, the pressure rise due to the incident shock is sensed upstream to the location where the incident shock would impact the wall because of slow acoustic waves, explaining the location of the separation point upstream of the impact location. At the separation point, the deviation of the supersonic flow due to the separation leads to the formation of the so called *reflected shock wave*. In fact, the incident shock is reflected at the boundary edge as expansion waves. At the reattachment point, the deviation of the supersonic flow due to the presence of the wall leads to compression waves that also coalesce to form the so called *reattachment shock-wave*. In this configuration, the viscosity at play in the boundary layer leads to a complete restructuring of the flow even in the outer region where a different system of shock waves is created, with respect to the inviscid Mach shock wave reflexions on a wall. For a more complete description of the flow topology, reader could refer to the work of J. Delery in [4].

The extent of the recirculation bubble is driven by the intensity of the incident shock wave, let say the pressure ratio from each side of the shock, and by the incoming boundary layer velocity profile. Indeed, the stronger the shock, the stronger the adverse pressure gradient leading to the separation of the boundary layer. Furthermore, the larger the normal to the wall velocity gradient within the boundary layer, the better the boundary layer is able to resist to the separation caused by the adverse gradient pressure. For instance, a laminar boundary layer is more prone to separation than a turbulent one when subjected to a steep adverse pressure gradient. The separation bubble extent then characterizes the interaction studied. The skin friction coefficient C_f is hence an important quantity as it allows us to determine the locations of the separation (where C_f becomes negative) and the reattachment points (where

C_f becomes positive again). The skin friction coefficient is defined as follows:

$$C_f = 2.\frac{\tau_w}{\rho_0 U_0^2}, \tag{21}$$

where $\tau_w = \mu_w \left.\dfrac{\partial u}{\partial y}\right|_{y=0}$ is the shear stress at the wall.

As described in [4] and recalled above, due to the strong shock wave boundary layer interaction studied here, a complex system of shock waves, compression and expansion waves is formed in the supersonic part of the flow. The accuracy of the calculation in this part of the flow depends greatly on the ability of the numerical scheme to capture discontinuities (shock waves) without spoiling the accuracy of the solution in the vicinity of discontinuities. In the following, we evaluate the efficiency of the present shock capturing procedure to predict the pressure distribution in the supersonic part of the flow.

All the following results of the steady laminar SWBLI are obtained after a complete convergence towards steady solutions up to the machine precision.

5.1 Grid convergence study.

Figure 11 shows the wall pressure and the skin friction coefficient distributions while figure 12 presents the pressure distribution at an altitude $y = 0.1$ for different mesh sizes obtained by using the OSMP-7 scheme coupled with a 2^{nd}-order centered scheme for the viscous fluxes. The different mesh sizes considered are 80×40, 200×100, 280×140, 360×180, and 480×240. The use of the limited version of the scheme OSMP-7 is first favored since a shocked flow is considered here.

A typical wall pressure distribution for such strong interaction is characterized by a first steep rise of the pressure associated with the reflected shock wave with a foot located at the separation point, followed by a plateau like of pressure characteristic of the closed separation bubble. A second wall pressure rise then occurs that is associated with the reattachment process, leading to the same pressure downstream of the reattachment as in the inviscid case. The wall pressure distribution is then an important quantity to assess the accuracy of the simulations.

The 80×40 mesh fails to recover the right behavior previously described since the mesh is not fine enough to capture the interaction. Regarding other meshes, the wall pressure distribution estimated by the numerical scheme is in good agreement with the theoretical considerations previously reminded: two steep rises of the wall pressure separated by a plateau like pressure. The wall

pressure values before and after the interaction are the same for each mesh size used and corresponds to the non-viscous values. Discrepancies between several meshes on the wall pressure distribution are noticeable inside the region of interaction. The finer the mesh, the earlier the first pressure rise, and the later the second pressure rise. A grid convergence is however observed towards a unique solution as the mesh is refined. The value and the extent of the plateau of pressure is nearly the same for every meshes.

We also observe a grid convergence towards a unique steady solution for the skin friction coefficient distribution shown in figure 11-right. The same observations as for the pressure distribution hold for the locations of the separation and the reattachment points in accordance with the mesh refinements.

The pressure distribution at $y = 0.1$ is shown in figure 12 for different meshes. At $y = 0.1$, which is in the non viscous region away from the separation, the pressure distribution clearly exhibits the locations of compression and expansion waves: a sharp compression corresponding to the incident shock followed by a continuous compression corresponding to the reflected compression waves. This continuous compression is followed by a sharp decrease of the pressure corresponding to the expansion waves coming from the top of the detachment bubble. This is followed by a continuous compression due to the compression waves relative to the reattachment of the boundary layer. Meshes of 80×40 and 200×100 grid points are not fine enough to correctly capture the rapid pressure evolutions, namely the shock wave and the expansion waves. For finer meshes, results converge towards a unique steady solution.

For the three quantities described (figures 11 and 12), very weak discrepancies can be exhibited between results on the 360×180 mesh and the 480×240 mesh. Therefore, we believe that the solution on the 480×240 mesh is the fully converged solution of this steady problem and the following analyses consider this configuration.

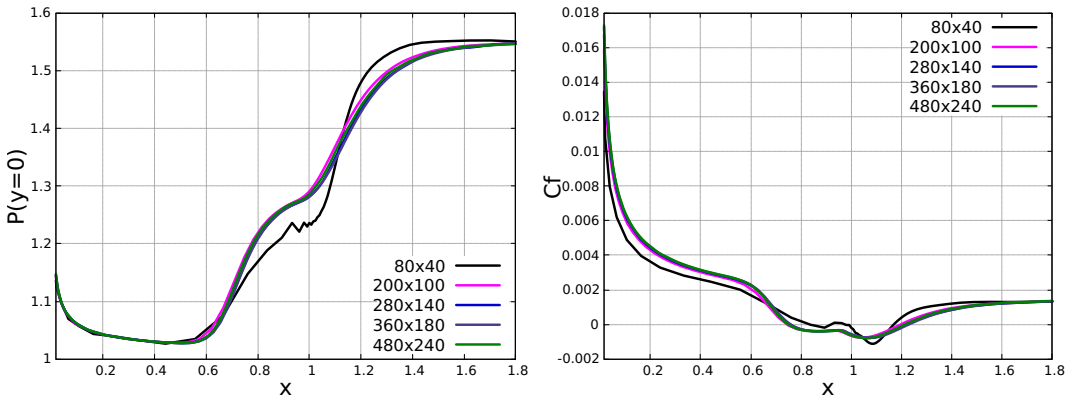

Fig. 11. Wall pressure (on the left) and skin friction coefficient (on the right) distributions obtained by using the OSMP-7 scheme coupled with a 2^{nd}-order centered scheme for the viscous fluxes, on several mesh sizes.

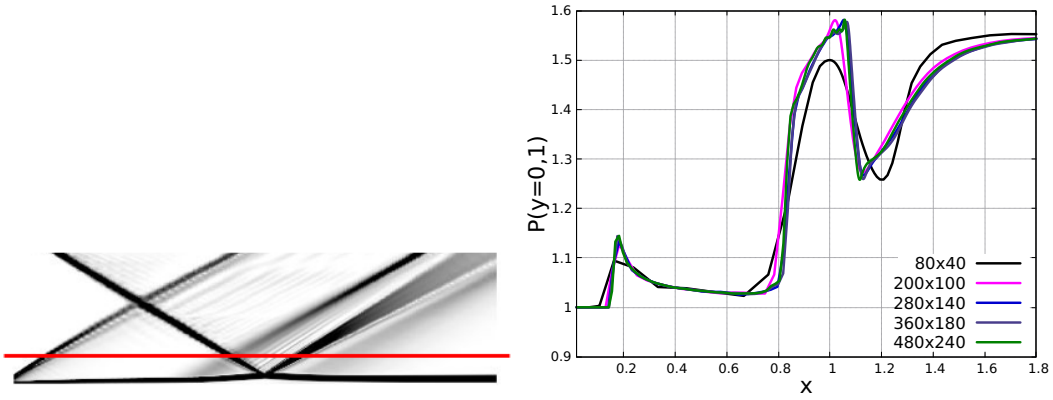

Fig. 12. On the left, numerical schlieren visualization obtained by using the OSMP-7 scheme coupled with a 2^{nd}-order centered scheme for the viscous fluxes, on 480×240 grid points: the red line indicates the height $y = 0.1$. On the right, pressure distribution at $y = 0.1$ obtained by using the OSMP-7 scheme coupled with a 2^{nd}-order centered scheme for the viscous fluxes, on several mesh sizes.

5.2 Effect of the MP constraints on the results.

The effect of using the OSMP-7 instead of the unlimited OS-7 scheme is highlighted in figures 13 and 14 in which results obtained using the OS-7 and OSMP-7 are plotted for the 480×240 mesh. As expected, the pressure distribution at $y = 0.1$ (figure 13-left) highlights that the use of the OS-7 scheme leads to spurious oscillations in the vicinity of discontinuities. These oscillations are almost cancelled when the shock capturing procedure (MP constraints) is activated, namely when the OSMP-7 scheme is used. No noticeable difference is observed for the wall pressure distribution between results obtained using the OS-7 and the OSMP-7 schemes away from shock waves. Thus, spurious pressure oscillations produced around the shock wave do not influence the wall pressure distribution. On the contrary, the skin friction calculated with the OS-7 scheme differs slightly from the skin friction coefficient calculated using the OSMP-7 scheme in the recirculation zone (figure 14), where oscillations are observed for the result using the unlimited scheme. It shows that the spurious oscillations created in the vicinity of the discontinuities influence the solution in the entire domain.

These results show that the MP constraints are efficient to recover a good quality of solutions without an extra cost since the simulation time when the MP constraints are used is only 2,7 % greater than for the unlimited OS scheme. This additional cost is almost negligible.

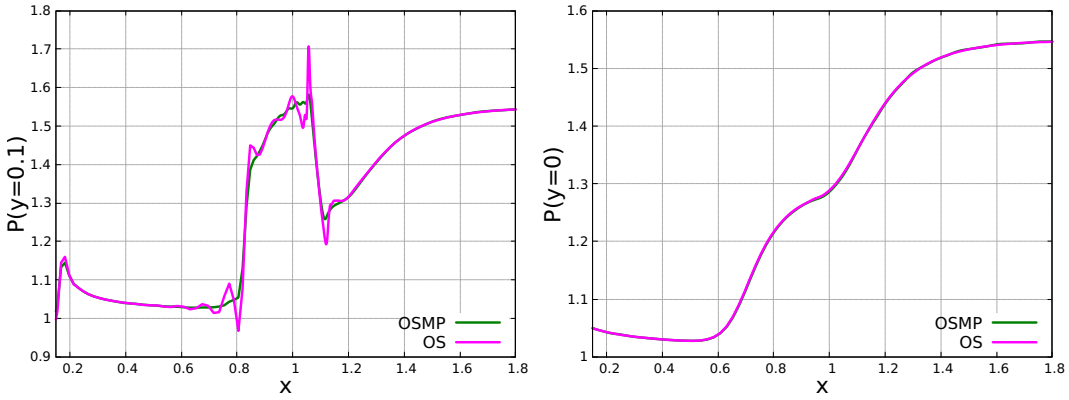

Fig. 13. Pressure distribution at $y = 0.1$ (on the left) and along the wall (on the right) for the 480×240 mesh: influence of the MP constraints.

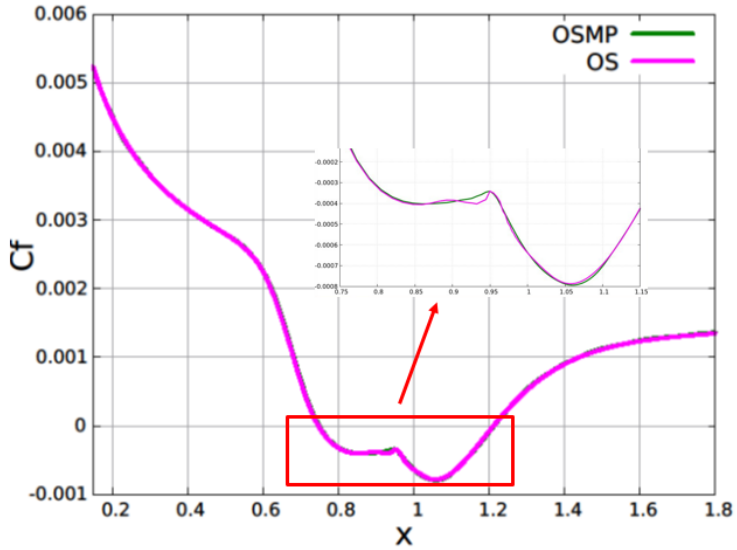

Fig. 14. Skin friction coefficient distribution along the wall for the 480×240 mesh: influence of the MP contraints.

5.3 Comparison of present results with numerical and experimental results from the literature.

Previous results are compared with either experimental or numerical results from the literature. Experimental results come from Degrez *et al.* [30] who designed the present test case. Degrez *et al.* also provided numerical results [30]. Other high-order numerical results have also been selected to compare with as they have been obtained with two numerical schemes commonly used to simulate compressible flows: the DNS of Gross and Fasel using a 9^{th} accurate WENO method based on the Van Leer (VL) flux vector splitting [33], and the

DNS of Blanchard and Renac performed in the framework of the HIOCFD workshop using a 6^{th} order Discontinuous Galerkin (DG) scheme [31].

The comparison of the wall pressure distributions is plotted in figure 15-left. It is noteworthy that the pressure levels before and after the interaction are the same for every results. The results using the OSMP-7 scheme match perfectly the results obtained by Blanchard and Renac [31], even in the interaction zone. Gross and Fasel [33] obtained results that seem more in agreement with the experimental results. The difference must be attributed to the inlet boundary condition that are based on a laminar boundary layer similarity solution on the opposite of uniform flow conditions prescribed for Blanchard and Renac and the present results. Besides, the pressure distribution at $y = 0.1$ obtained with OSMP-7 scheme is compared with the distribution provided by Blanchard and Renac [31] in figure 15-right. No shock capturing technique is used in the DNS of Blanchard and Renac explaining the spurious oscillations in the vicinity of discontinuities. Slopes of the pressure variations as well as locations of the shock wave, the expansion waves and the reattachment recompression agree very well in both simulations.

Streamwise distributions of the skin friction coefficient are compared in figure 16. Experiments of Degrez *et al.* [30] only provided measured locations of the separation and the reattachment points. Results obtained using the OSMP-7 scheme is one more time in good agreement with results of Blanchard and Renac [31]. One more time, results provided by Gross and Fasel [33] agree well with the experiments. The fact that the inlet conditions used by Gross and Fasel are different from ours influence the development of the boundary layer and then the distribution of the shear stress along the plate.

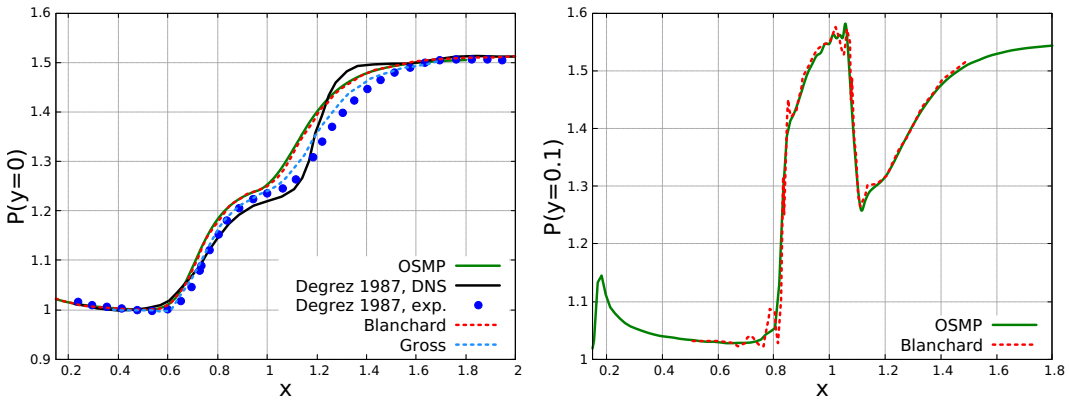

Fig. 15. Streamwise pressure distribution obtained either from experiments or by using several schemes: wall pression on the left, and pressure at $y = 0.1$ on the right.

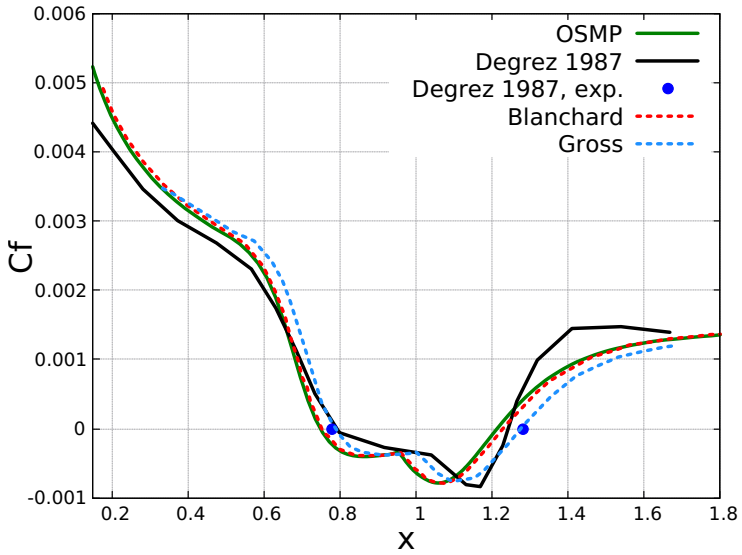

Fig. 16. Streamwise skin friction coefficient distribution obtained either from experiments or by using several numerical approaches.

5.4 Influence of the order of accuracy of the diffusive fluxes

Results obtained using the OSMP-7 scheme coupled with a 4^{th}-order centered finite difference approximation for the diffusive fluxes are compared with those using a 2^{nd}-order centered finite difference approximation. The comparison is only performed on the skin friction coefficient distribution because it is more sensitive than the pressure to the order of accuracy of the viscous fluxes discretization. No difference is noticeable between these results, even for quantities calculated close to the wall where viscosity plays a dominant role. It shows that, using this mesh, a 2^{nd}-order centered finite difference approximation for the diffusive fluxes is sufficient to accurately simulate the present flow at such high Reynolds number.

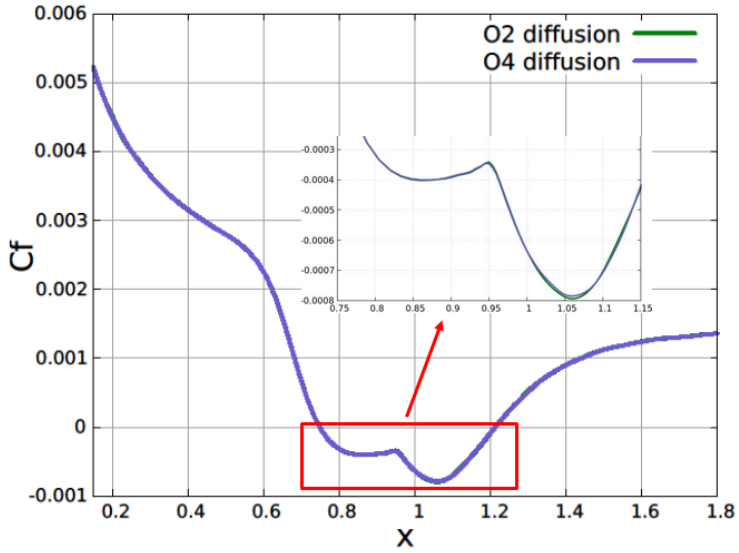

Fig. 17. Skin friction coefficient distribution for the 480×240 mesh obtainted by using either a 2^{nd}-order or a 4^{th}-order approximation for the diffusive fluxes.

6 Shock wave turbulent boundary layer interaction (SWTBLI)

In previous sections (4 and 5), the ability of the solver to compute turbulent and shocked flows has been evaluated separately on canonical test cases. In this section, we aim at evaluating the ability of the solver to compute a flow in which these two characteristics interact: namely a strong shock wave turbulent boundary layer interaction (SWTBLI).

6.1 Dynamics of the SWTBLI

The flow organization introduced in section 5 corresponds to the mean organization of strong interactions. The strong SWTBLI are however unsteady. The dynamic features of strong SWTBLIs are characterized by several unsteady phenomena whose characteristic scales spread over a large broadband spectrum range. Main phenomena are listed below.

6.1.1 High frequency features

For SWTBLI, the incoming boundary layer is turbulent with the most energetic fluctuations at high frequencies characterized by a Strouhal number $St_\delta = \dfrac{f\delta}{U_e} \sim 1$ (where f, δ and U_e are respectively the main frequency of

the fluctuations, the boundary layer thickness before the interaction and the free stream velocity). Low amplitude oscillations of the reflected shock wave have been observed in several numerical simulations of strong SWTBLIs (for instance [34]) at the same frequency scale as the most energetic fluctuations of the incoming boundary layer (i.e. at high frequency). As explained in [35], these small unsteady ripples of the reflected shock waves were also observed in simulations of weak interactions, for which no separation of the boundary layer occur. These high frequency oscillations of the reflected shock waves are then linked to the incoming turbulence whose most energetic scales excite the reflected shock wave.

6.1.2 Medium frequency features

The dynamics of subsonic separated and reattached flows have been extensively studied and characteristic frequency ranges have been educed ([36,37,38]). In particular these studies highlighted that the shear layer bounding the upper part of the separation bubble, is subjected to two instabilities of medium characteristic frequencies. The shear layer is submitted to a convective instability (Kelvin-Helmholtz waves) whose non-linear evolution leads to a vortex shedding at a Strouhal number around $St_L = \frac{fL}{U_e} \simeq 0.6 - 0.8$ based on the length (L) of the recirculation bubble. The shear layer is also submitted to an absolute instability called *"flapping"* of the shear layer that has the characteristic frequency $St_L = \frac{fL}{U_e} \simeq 0.12 - 0.15$. This flapping phenomenon comes from successive enlargement and shrinkage of the recirculation bubble. The shrinkage is associated to a vortex shedding downstream of the recirculation bubble.

6.1.3 Low frequency features

For supersonic flows, a low frequency flapping mode of the recirculation bubble has also been observed in addition to the medium frequency flapping at a Strouhal number of $St_L = \frac{fL}{U_e} \simeq 0.03 - 0.04$ ([39] [40]). This low frequency flapping mode is also called the *"breathing"* of the separation bubble. A low frequency oscillation of the whole SWTBLI system (the recirculation bubble in phase with the system of shock waves) is also observed in simulations and experiments ([4]). This instability, called the *"unsteadiness"* of the SWTBLI, consists in an oscillation of the recirculation bubble coupled to the shock wave system. This low frequency phenomenon has the same characteristic Strouhal number as the breathing of the separation bubble, namely $St_L = \frac{fL}{U_e} \simeq 0.03 - 0.04$ [4].

6.2 Physical parameters, computational domain and mesh.

For this simulation, the OSMP 7^{th} order scheme has been employed. Following results obtained in sections 4 and 5, a 2^{nd}-order approximation is also used for the viscous flux discretization. The negligible influence of higher order discretization of the viscous fluxes is further confirmed in appendix A for wall bounded flows.
A sketch of the flow is given in figure 18. No-slip and adiabatic conditions are prescribed at the wall of the flat-plate. Outlet time dependent non-reflecting boundary conditions are imposed at the outlet boundary. Periodic boundary conditions are imposed in the spanwise direction (z). In order to lower the numerical cost associated to the simulation of turbulent boundary layers, synthetic turbulent boundary conditions have been employed at the inlet of the domain. It consists in a Synthetic Eddy Method (SEM) [24,25] that we adapted to compressible flows. The flow conditions are taken from [41] and physical parameters of the boundary layer are summarized in table 1. The inlet conditions are extensively presented in appendix A, where the simulation of a compressible turbulent boundary layer with the same physical parameters as the one considered in [41].

A shock wave with an angle of 33.2° (corresponding to a flow deviation of 9.25° through the shock wave) is created by imposing the Rankine-Hugoniot relationship at the top boundary of the domain at $x/\delta = 14.07$ (see figure 18). The shock wave impinges the boundary layer at $x/\delta \simeq 39.5$. At this abscissa along the flat plate, the boundary layer created using the SEM is in a fully turbulent state (see appendix A).

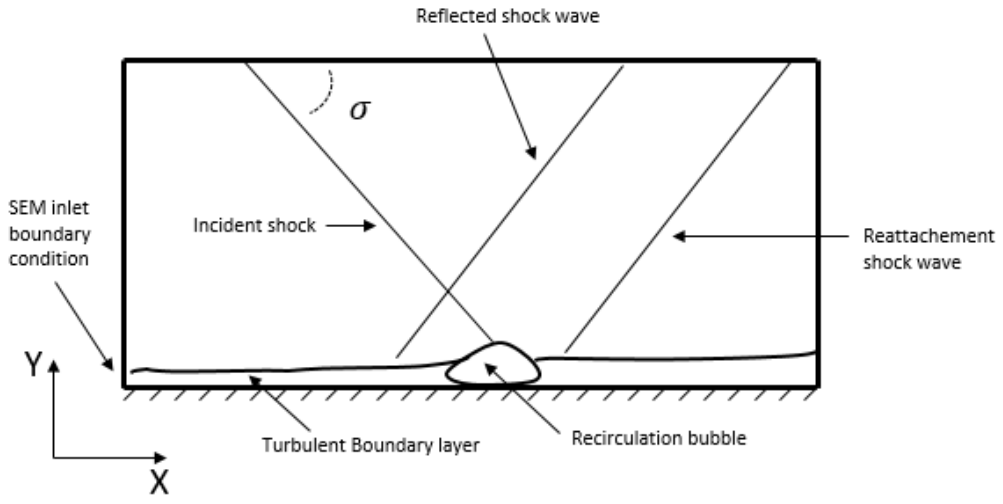

Fig. 18. Sketch of the flow.

Table 1
Flow conditions for the DNS of the SWTBLI.

M_∞	U_∞ (m/s)	P_∞ (Pa)	T_∞ (K)	T_w (K)
2.33	556	2351.11	141.71	269.75

δ (m)	θ (m)	Re_δ	Re_θ
5.3×10^{-3}	7.68×10^{-4}	17520.21	2538.78

A structured mesh of size 785×313×113 cells in $(x \times y \times z)$ is used to discretize a 3D domain of simulation that has an extent of 60.4 δ ×16.7 δ× 3 δ, with δ the boundary layer thickness at the inlet of the domain (see Table 1). The mesh used is refined near the wall in the normal to the wall direction (y). The minimum grid spacing at the wall is $\Delta y_w^+ \simeq 0.9$ in the boundary layer before the interaction region (for $x/\delta = 20$). A uniform mesh is used in the longitudinal and spanwise directions (respectively x and z) with a grid spacing of $\Delta x^+ \simeq 18.3$ and $\Delta z^+ \simeq 6.3$. This grid resolution is similar to the grid resolution used in appendix A for the validation of the SEM.

6.3 Numerical results

6.3.1 Turbulent boundary layer state upstream of the interaction.

A compressible turbulent boundary layer has been simulated using the SEM procedure that is extensively presented in appendix A. To present the state of the turbulent boundary layer upstream of the interaction, figure 19 shows a comparison between results obtained in the current DNS and results of [41] for the velocity profile and the Reynolds stress tensor ($R_{ij} = \dfrac{\overline{\rho} \widetilde{u_i'' u_j''}}{\overline{\rho}_w u_\tau^2}$) profile with respect to y^+ (in wall units). Both the velocity and the Reynolds stress profiles are in good agreement with the reference values obtained from [41]. The trends generally admitted for the Reynolds stress profiles in the inertial region [42] are also very well recovered, mainly for R_{33} that better fits the trend than Mullenix and Gaitonde results [41], and for R_{12} that recovers a plateau evolution at a value -1 that is fully consistent with the energetic equilibrium assumption.

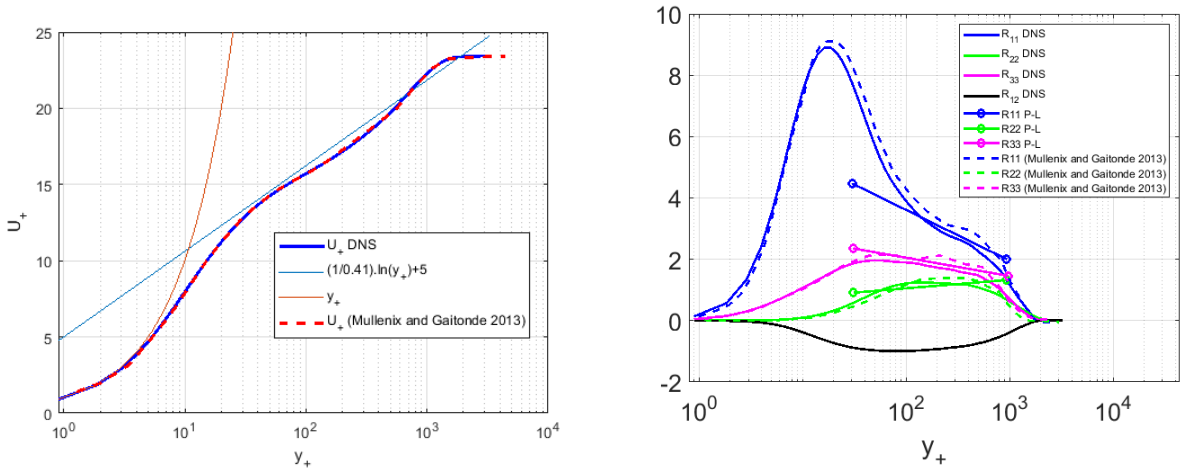

Fig. 19. Comparison between the SEM and the results from [41] for $Re_\theta \simeq 3500$ and $x/\delta = 62.5$. Left: Velocity profiles in the Van Driest transformed coordinates. Right: Density-scaled Reynolds stresses. The trend lines are from [42].

Figure 20 shows a comparison between the temperature profile obtained in the current DNS and the reference result of [41]. The profiles are in good agreement showing the ability of the numerical approach (numerical scheme + fine mesh + SEM) to accurately compute thermodynamic fields. We can note that the gradient of T in the normal wall direction is clearly zero at the adiabatic wall.

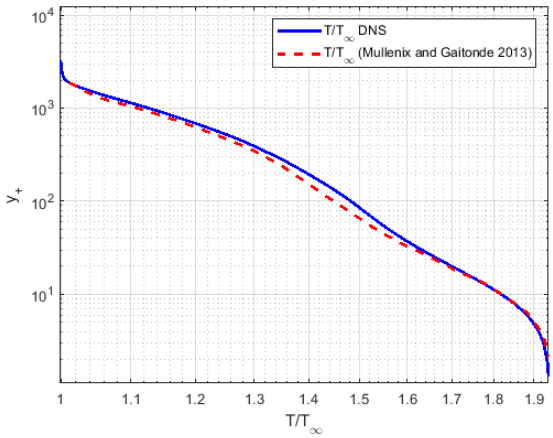

Fig. 20. Comparison between the SEM and the results from [41] for $Re_\theta \simeq 3500$. Temperature profile.

6.3.2 Mean flow organization

A numerical Schlieren visualization (2D (x, y) plane located at $z/\delta = 1.5$) is shown in figure 21. We clearly see the development of the turbulent bound-

ary layer, that is progressively thickened before the interaction zone occurs. A Mach line is also visible, originating from the flat plate at the upstream inlet boundary. This Mach line is present because of the adaptation of the modeled turbulent profile to the presence of the wall. This visualization also highlights the brutal increase of the boundary layer thickness through the interaction. The overall shock wave system organization of a SWTBLI described in [4], briefly recalled in section 5, is recovered. Indeed, due to the strong incident shock-wave impingement, the boundary layer separates. A closed recirculation bubble (highlighted in figure 22 of the mean streamwise velocity) is created as well as the subsequent reflected shock wave. The reattachment of the boundary layer leads to compression waves that are clearly visible in the numerical Schlieren visualization.

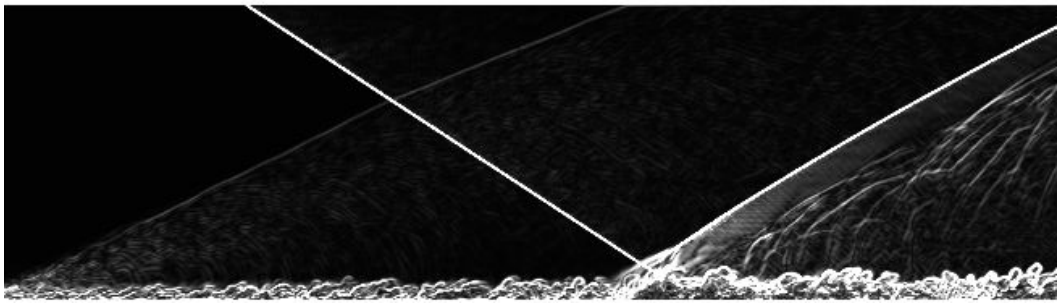

Fig. 21. Numerical schlieren visualization (2D slice located at the middle of the domain).

Figure 22 shows a comparison between the time mean streamwise and normal to the wall velocities averaged in the spanwise direction in the interaction region obtained for the current DNS. The current results are compared to results of simulations of [43] of the SWTBLI between the same compressible turbulent boundary layer and a shock wave characterized by a deviation of the flow of 9° (the strength of the shock is slightly lower than in our simulation). Velocities are scaled using U_∞ and the spatial coordinates are scaled using the inlet boundary layer thickness (δ). Computations of the time means of fields are performed over a simulation time of about 12 cycles of the low frequency unsteadiness corresponding to $\Delta t = 360\dfrac{L}{U_\infty}$. The time averaging is started after the transient phase corresponding to the creation of the shock wave system and the recirculation bubble. The presence of a mean separation bubble is highlighted by the reverse flow region characterized by negative longitudinal velocity. An overall agreement is found between the two simulations. Moreover, some details obtained by [43] using the finer mesh are caught by the current DNS. It is particularly visible in the expansion fan after the shock impingement where the velocity variations computed in the current DNS match the details captured by the fine grid in the simulations of [43].

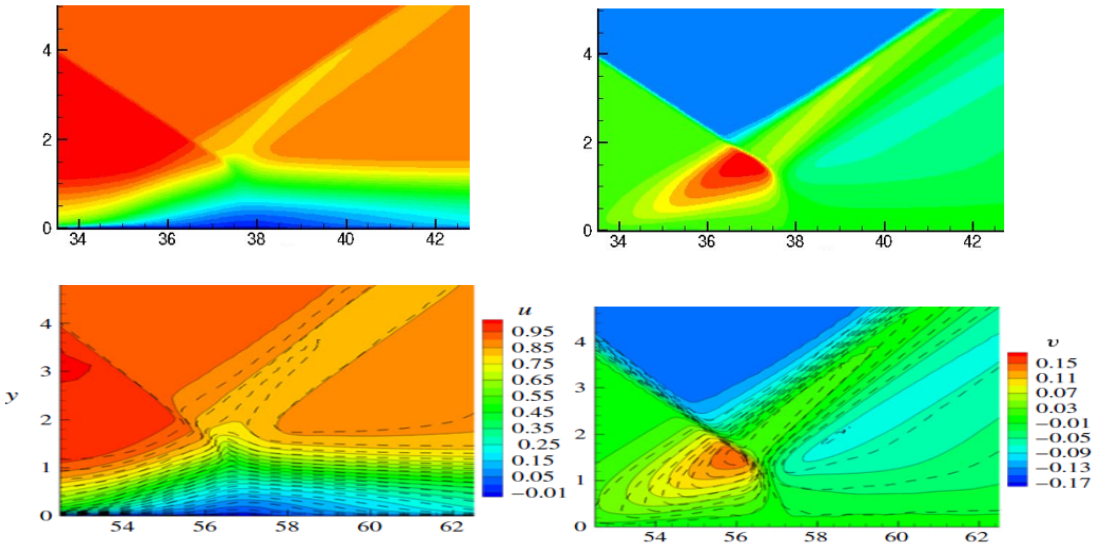

Fig. 22. Time mean velocity averaged in the spanwise direction in the interaction zone. Up left: longitudinal velocity (current DNS), Up right: vertical velocity (current DNS), Bottom left: longitudinal velocity (from [43]), Bottom right: vertical velocity (from [43]). For the results from [43], the color contours correspond to a coarser mesh ($\Delta x^+ = 23.5$, $\Delta y_w^+ = 0.4$, $\Delta z^+ = 8.9$), whereas the dashed contour lines correspond to a finer mesh solution ($\Delta x^+ = 16.4$, $\Delta y_w^+ = 0.4$, $\Delta z^+ = 6.1$).

The time mean value of the skin friction coefficient (C_f) averaged in the spanwise direction is shown in figure 23. The mean abscissa of the separation point can be defined as the abscissa for which this curve becomes negative, and we obtain $\overline{X}_s = 34.21\delta$. The mean abscissa of the reattachment point can be defined as the abscissa for which this curve becomes positive again, and the location is $\overline{X}_r = 39.13\delta$. The mean separation length can then be defined as the difference $\overline{X}_r - \overline{X}_s$. We obtain $L = 4.92\delta$. This value is to be compared to the mean separation length of 4δ obtained by [43]. The lower value of the mean separation length obtained by [43] is consistant with the lower strength of the shock in their simulation than in our present configuration.

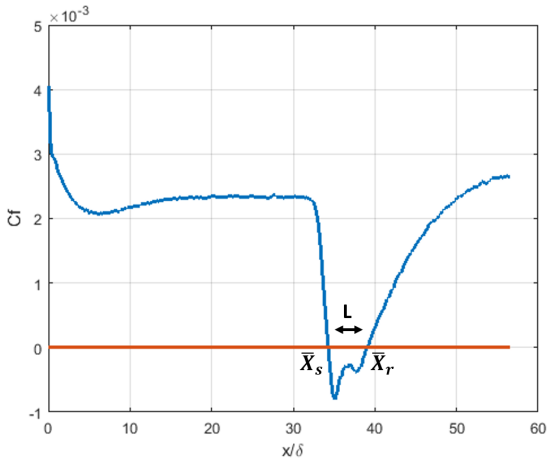

Fig. 23. Time mean C_f averaged in the spanwise direction with respect to x/δ. L denotes the mean separation length, $\overline{X}_s$ denotes the mean separation point and $\overline{X}_r$ denotes the mean reattachment point.

The time mean values of the wall pressure and the skin friction coefficient averaged in the spanwise direction are respectively shown in figures 24 and 25. Values are compared with results from [43]. The strength of the shock wave being slightly smaller in the SWTBLI simulated by [43] than in the current DNS, some discrepancies are observed. The pressure rise is sharper in the current simulation than in [43], which is consistent with the higher pressure ratio of the SWTBLI. The skin friction coefficient upstream of the interaction appears to be lower in the simulation of [43] than in the current DNS. This discrepancy between values of the skin friction coefficient upstream of the interaction is in contradiction with results from [41], presented in appendix A for the same boundary layer in which perfect agreement was obtained for the skin friction coefficient. Results from [43] are therefore not consistant with results from [41] and must therefore be interpreted with caution. Within the separation, discrepancies are also recorded between skin friction distributions. The skin friction distribution within the separation bubble reported in [43] is more intense (with lower skin friction values) than the one obtained in our DNS. Moreover, two local minima are observed in the skin friction distribution obtained in our DNS. This behavior, not observed in the results reported by [43] is also observed in other studies such as [8]. Discrepancies observed between skin friction coefficients can be attributed to the difference in the grid resolution between the two simulations. Indeed, the mesh used in [43] ($\Delta x^+ = 23.5$, $\Delta y_w^+ = 0.4$, $\Delta z^+ = 8.9$) is coarser than our mesh in the longitudinal and spanwise directions. In [44], a study of the skin friction variability between different studies concluded that the skin friction distribution in the separated zone is particularly sensitive to the grid refinement in the longitudinal direction.

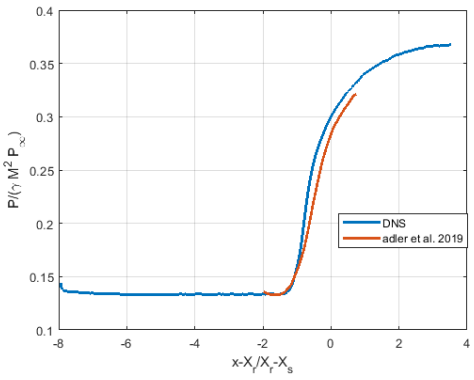

Fig. 24. Time mean pressure averaged in the spanwise direction with respect to $(x - \overline{x}_r)/(\overline{x}_r - \overline{x}_s)$.

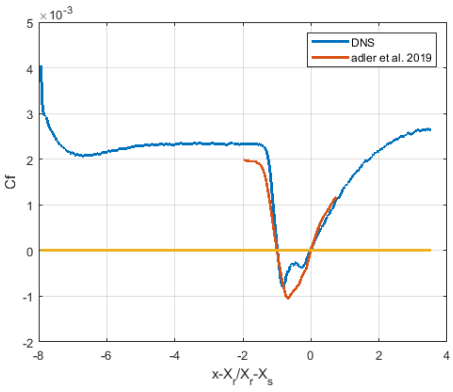

Fig. 25. Time mean C_f averaged in the spanwise direction with respect to $(x - \overline{x}_r)/(\overline{x}_r - \overline{x}_s)$.

These results show that the OSMP scheme is able to recover mean properties of the SWTBLI consistent with the results from the literature (mainly, for instance, with [8,44]).

6.3.3 Dynamics of the interaction

We now focus on results obtained for the dynamics of the interaction. In particular, we are interested in verifying the ability of the OSMP scheme to recover commonly admitted dynamics behavior of strong SWTBLIs such as the low frequency breathing of the recirculation bubble and the low frequency unsteadiness of the reflected shock wave.

Histories of the separation and reattachment point abscissa averaged in the spanwise direction (respectively x_s and x_r) are plotted in figure 26. x_s corresponds to the most upstream abscissa at which the skin friction coefficient becomes negative. x_r corresponds to the most downstream abscissa at which the skin friction coefficient becomes positive again. Alternatively to the definitions of the mean abscissa of the separation and reattachment point previously given in the description of figure 23, these quantities can be defined respectively as the time mean of x_s and x_r. We obtain $\overline{x}_s \simeq 34.25\delta$ and $\overline{x}_r \simeq 40.9\delta$. The amplitude of the reattachment point motion is significantly larger than the amplitude of the separation point motion. This is in accordance with results obtained by other authors ([8], [44]). The power spectral densities of these two signals have been computed and are shown in figure 27. The reattachment point is dominated by frequencies characteristic of the medium frequency ($St_L \simeq 0.15$) and low frequency ($St_L \simeq 0.03 - 0.05$) flapping of the shear layer, the medium frequency being more energetic. The motion of the

separation point is dominated by the low frequency activity of the recirculation bubble and is characterized by the presence of very low frequency activity ($St_L \simeq 0.015$).

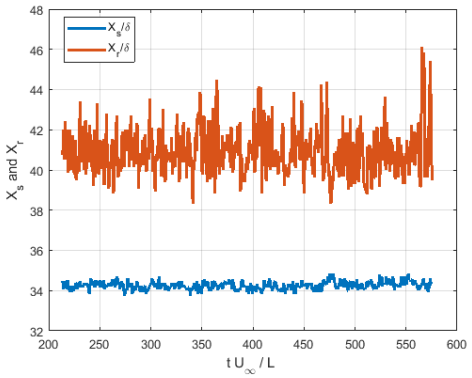

Fig. 26. Time history of the spanwise averaged locations of the separation point $x_s(t)$ and the reattachment point $x_r(t)$

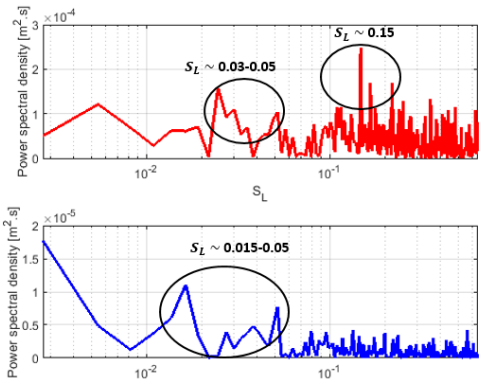

Fig. 27. Power spectral density of the time history of the spanwise averaged location of the separation point $x_s(t)$ (red) and the time history of the spanwise averaged location of the reattachment point $x_r(t)$ (blue).

Figure 28 shows the history of the separation point location along the flat plate and the history of the position of the reflected shock waves foot X_{shock}. As in [44], the position of the shock wave is identified at each time of acquisition as the abscissa for which the wall pressure becomes 30% bigger than P_∞. The standard deviation of X_{shock} is 0.16δ. The covariance of $X_s(t)$ and $X_{shock}(t)$ is shown in figure 29 highlighting the high correlation between the motions of the separation point and the reflected shock wave.

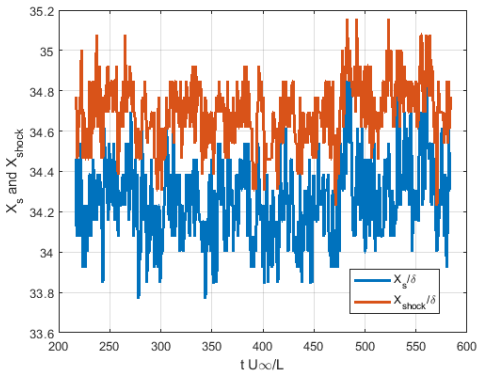

Fig. 28. Time history of the spanwise averaged location of the separation point $x_s(t)$ and the reflected shock foot $X_{shock}(t)$.

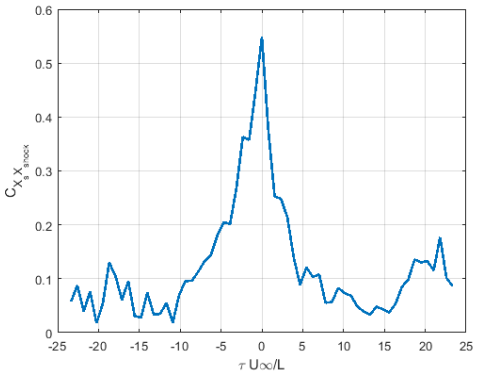

Fig. 29. Distribution of the covariance between $x_s(t)$ and $X_{shock}(t)$ as a function of the non dimensionalized time lag $\tau U_\infty/L$.

These results show that the medium and low frequencies of the recirculation bubble is recovered by our simulation, associated to the low frequency unsteadiness of the reflected shock wave.

7 Conclusion and perspectives

In the present study, the ability of the high order OSMP scheme to accurately compute wall bounded turbulent shocked flows has been studied.

As a first step, the ability of the scheme to compute turbulent and shocked flows has been studied separately. It has first been performed by simulating an unbounded turbulent flow which fairly closely mimics the energy cascade found in Homogeneous Isotropic Turbulence (HIT): namely the 3D Taylor-Green vortex. Results demonstrate the correct accuracy of the OSMP scheme to predict turbulent features. In particular, the effect of the MP constraint on results has been shown to be negligible for a such unbounded *"smooth"* turbulent flow. It testifies to the robustness of the MP procedure that doesn't degrade the accuracy of the solution away from discontinuities. Moreover, an order of accuracy higher than 2^{nd}-order for approximating the diffusive fluxes seems to have a negligible influence on the solution for such relatively high Reynolds numbers. We also showed that the OSMP scheme is completely competitive compared to the best result obtained on this well-known test case at the 4-th High-Order CFD Workshop [29] with an overall error on the kinetic energy dissipation of about one order lower for the same grid resolution.

Secondly, the simulation of a 2D steady SWLBLI has shown the great efficiency of the MP procedure to capture discontinuity without spoiling the solutions.
The DNS of a wall bounded turbulent shocked flow has then been undertaken. A Synthetic Eddy Method, that we adapted to the compressible regime, has been implemented to prescribe an inlet boundary condition capable of initiating a fully developed turbulent boundary layer without prohibitive additional computational costs. The results are in very good agreement with the reference results. An adaptation length of about 20 initial boundary layer thicknesses (δ) has been found sufficient to recover realistic values of the skin friction coefficient, realistic velocity and Reynolds stress profiles, that is found to be very small compared to other existing methods. Moreover, even for this bounded flow, the use of an order of accuracy higher than the 2^{nd}-order for approximating the diffusive fluxes was shown to have a negligible influence on the solution, even close to the wall. Results obtained for the SWTBLI simulation are in accordance with reference solutions from the literature, both for the mean properties and the dynamics features of the flow. In particular, the low frequency breathing of the recirculation bubble and the low frequency oscillations of the reflected shock wave have been captured by our simulation.

The OSMP scheme with a 2^{nd}-order approximation of the diffusive fluxes and the SEM adapted for compressible flows is then a reliable numerical tool for the simulation of wall bounded turbulent shocked flows. It is then with confidence that we can undertake much deeper physical analyses of the interaction of shock waves with turbulent boundary layer that will be the next step of this work.

Acknowledgment:

This work was granted access to the HPC resources of IDRIS under the allocation A0052A07195 made by GENCI (Grand Equipement National de Calcul Intensif). Authors greatly thank this institution. Authors would like to also gratefully thank Marta Garcia-Gasulla, Victor López, and Guillaume Houzeaux from the Barcelona Supercomputing Center for having optimized the SEM implementation in CHORUS software in the framework of the European Performance Optimisation and Productivity Centre of Excellence in HPC (POP CoE, GA n. 824080).
Ismaïl BEN HASSAN SAÏDI was granted by École Doctorale SMEMaG, Université Paris-Saclay.

Appendices

A Direct numerical Simulation of a compressible turbulent boundary layer

In this appendix, we evaluate the ability of the OSMP scheme to compute wall bounded compressible turbulent flows. Namely, the simulation of a compressible turbulent boundary layer is presented. We first present the turbulent inflow implemented in order to lower the numerical costs associated to this simulation. The results are then presented and compared to a reference solution.

A.1 Turbulent inflow

In order to lower the numerical cost associated to the simulation of turbulent boundary layers, turbulent inlet boundary conditions have been developed and are available in the literature. Some methods consist in accelerating the destabilization of a laminar boundary layer imposed at the inlet of the domain [10,8]. Other methods consist in feeding the inlet of the domain with unsteady boundary conditions representative of the turbulent boundary layers. Reviews on this subject can be found in [45,46,47]. Among these methods, the Synthetic Eddy Method (SEM) has first been developed for incompressible flows [24] and then been improved by [25] for its use in the context of wall bounded flows. In this study, we implemented the SEM presented in [25], adapted for compressible flows.

In the following, the variables are decomposed using a Reynolds decomposition $f = \overline{f} + f'$ where $\overline{f}$ denotes the ensemble average of f and f' fluctuations of f centered on the mean ($\overline{f}$).

A.1.1 Prescription of the velocity at the inlet of the domain

The SEM uses the Cholesky decomposition $A_{ij}(y)$ of a prescribed Reynolds stress tensor $R_{ij}(y)$ to assign second order moments to a normalized stochastic signal $\widetilde{u}_j(y,z,t)$ superimposed to a mean velocity profile $\overline{u}_i(y)$ at the inlet of the domain. The velocity signal at the inlet of the domain then writes:

$$u_i(y,z,t) = \overline{u}_i(y) + \underbrace{\sum_j A_{ij}(y)\widetilde{u}_j(y,z,t)}_{u_i'(y,z,t)}, \quad i = 1,2,3, \tag{A.1}$$

where $u_i'(y,z,t)$ are velocity fluctuations in each direction.

This operation proposed in [48] allows to prescribe both first and second order moments at the inlet of the domain if $\widetilde{u}_j(y,z,t)$ is a centered random sequence with unit variance and zero covariance: $\overline{\widetilde{u}_i \widetilde{u}_j} = \delta_{ij}$, where δ_{ij} is the Kronecker symbol ($\delta_{ij} = 1$ if $i = j$, $\delta_{ij} = 0$ otherwise).

$$\mathbf{A} = \begin{bmatrix} \sqrt{(R_{11})} & 0 & 0 \\ R_{21}/A_{11} & \sqrt{(R_{22} - A_{21}^2)} & 0 \\ R_{31}/A_{11} & \dfrac{R_{32} - A_{21}A_{31}}{A_{22}} & \sqrt{R_{33} - A_{31}^2 - A_{32}^2} \end{bmatrix}, \tag{A.2}$$

where $R_{ij} = \overline{u_i' u_j'}$ denotes the components of the Reynolds stress tensor. As seen in equation A.1, the SEM needs three inputs: the mean velocity profile, the Reynolds stress tensor at the inlet of the domain and a random signal $\widetilde{u}_j(y,z,t)$. In the following, we will introduce these three inputs of the SEM as they have been implemented for this study.

The mean velocity profile of the boundary layer at the inlet of the domain is prescribed using the analytical approximation introduced in [49] as detailed in appendix C.

The determination of the Reynolds stress tensor at the inlet of the domain requires knowing the fluctuating velocity field. As this information is not available, we impose approximate Reynolds stress components derived from the mean velocity profile using the Boussinesq hypothesis:

$$-\overline{u'v'} = \nu_t(\frac{\partial U}{\partial y}), \tag{A.3}$$

where ν_t is the turbulent viscosity.

The mixing length model is used in order to evaluate the turbulent viscosity:

$$\nu_t = l^2 D^2 \frac{\partial U}{\partial y}, \tag{A.4}$$

where l is the mixing length and D is the wall damping function. These functions are evaluated as follows [50]:

$$l = 0.085\delta \tanh(\frac{\chi}{0.085}\frac{y}{\delta}) \quad \text{with} \quad \chi = 0.41, \tag{A.5}$$

$$D = 1 - e^{(y^+/26)}, \tag{A.6}$$

where δ is the boundary layer thickness at the inlet of the domain. δ is defined as the distance from the wall at which the velocity reaches $0.99U_\infty$.

The value of the turbulent kinetic energy profile $k = \frac{1}{2}\sum_{i=1}^{3}\overline{u_i'^2}$ is then derived using the assumption of [51] and [52] that the ratio between k and $\overline{u'v'}$ is a constant:

$$k = \frac{-\overline{u'v'}}{\sqrt{C_\mu}}, \tag{A.7}$$

where the structure parameter C_μ has a generally admitted value $C_\mu = 0.09$.

We then use the Wilcox's hypothesis [53] to evaluate the value of the diagonal components of the Reynolds stress tensor.

$$\overline{u'^2} = \frac{4}{9}2k,\ \overline{v'^2} = \tfrac{2}{9}2k,\ \overline{w'^2} = \tfrac{1}{3}2k. \tag{A.8}$$

Finally, we impose $\overline{u'w'} = 0$ and $\overline{v'w'} = 0$. The Wilcox's hypothesis allows to take into account the turbulence anisotropy in a boundary layer and has been shown to provide good approximations throughout the log-law layer and most of the defect layer for zero pressure gradient boundary layer [53].

To generate the random signal $\widetilde{u}_j(y, z, t)$, we follow the approach introduced in [25], where the original SEM has been extended to account for the inhomogeneity of scales in the direction normal to the wall for boundary layer computations. Using this approach, the inlet plane is split into Þ zones in which the random signal has different scales.

The random signal $\widetilde{u}_j(y, z, t)$ is then computed as a sum over the Þ zones,

$$\widetilde{u}_j = \sum_{p=1}^{\text{Þ}} \widetilde{v}_{jp}, \tag{A.9}$$

where $\widetilde{v}_{jp}$ are normalized random signals that have compact support on the p^{th} zone and are referred to as modes. The construction of these modes is introduced in details in appendix D.

A.1.2 Prescription of the temperature and the density fields at the inlet of the domain

As a compressible Navier-Stokes system is solved, turbulent inflow conditions have to be provided also for the density and the temperature.

The mean temperature profile prescribed at the domain inlet is determined from the mean velocity profile using the Crocco's formula [50]. Assuming that the Prandtl number $Pr = 1$ and the turbulent number $Pr_t = 1$, this

formula links the mean static enthalpy profile with the mean velocity profile following:

$$h = h_w + (h_{i\infty} - h_w)\frac{U}{U_\infty} - (h_{i\infty} - h_\infty)(\frac{U}{U_\infty})^2 \tag{A.10}$$

where h is the static enthalpy, h_i is the total isentropic enthalpy, the index "w" denotes the variable estimated at the wall location, and the index ∞ denotes the free stream quantities.

Assuming an adiabatic wall, $h_w = h_{i\infty}$ and the Crocco's formula (A.10) becomes:

$$h = h_{i\infty} + (h_{i\infty} - h_\infty)(\frac{U}{U_\infty})^2 \tag{A.11}$$

This hypothesis is convenient. Indeed, avoiding h_w allows to impose the enthalpy profile knowing only the free stream conditions.

As we assume a perfect gas, equation (A.11) relates directly the mean temperature profile and the mean velocity profile.

The mean density profile is then derived from the mean velocity profile, using the perfect gas equation of state. For supersonic boundary layers over adiabatic walls, there is an experimental evidence of quasi constant total enthalpy profile if the Mach number is not too high (let say $M_\infty < 5$). It can then be assumed a zero total enthalpy fluctuations in the boundary layer ($h_i' = 0$). This hypothesis leads to the Strong Reynolds Analogy (SRA) [[50]]:

$$\frac{T'}{T} \simeq -(\gamma - 1)M^2 u' U \tag{A.12}$$

where T' is the temperature fluctuation and u' the longitudinal velocity fluctuation.

Moreover, for compressible turbulent boundary layers until $M_\infty \leqslant 5$ the velocity fluctuations are subsonic and experimental evidences show that pressure fluctuations and $\rho' T'$ are second order terms. This leads to:

$$\rho' = -\rho\frac{T'}{T} \tag{A.13}$$

where ρ' are the density fluctuations.

Relations (A.12) and (A.13) are used for prescribing temperature and density fluctuations at the inlet. This approach has also been used by [9] and [54].

A compressible turbulent boundary layer has been simulated using the SEM procedure introduced in the previous section. The OSMP-7 scheme is here employed. Following results obtained in section 4.3, 2^{nd}-order discretization is used for the viscous fluxes. The flow conditions are taken from [41] and summarized in table 1.

We employ a structured mesh of size $1033 \times 105 \times 113$ in $(\mathbf{x} \times \mathbf{y} \times \mathbf{z})$ to discretize the domain of simulation that has an extent of $80\delta \times 4\delta \times 3.0\delta$. In the normal to the wall direction, the mesh is tightened close to the wall using a hyperbolic tangent law to ensure a minimum grid spacing at the wall $\Delta y_w^+ = 0.9$ (at $x/\delta = 20$). A uniform mesh is used in the longitudinal and spanwise directions (respectively x and z) with a grid spacing of $\Delta x^+ \simeq 18.3$ and $\Delta z^+ \simeq 6.3$.

A snapshot (Q criterion colored by the longitudinal velocity between $x = 0$ and $x = 40\delta$) of the turbulent boundary layer obtained using this method is shown in figure A.1. The injection of eddies at the inlet of the domain is visible. As show in figure A.2, where the longitudinal velocity contours are plotted in a (x, z) plane at $y^+ \simeq 15$ above the wall, the boundary layer is populated by structures elongated in the streamwise direction close to the wall. Eddy ejections within the boundary layer is also clearly visible in figure A.1 in the form of hairpin vortices. The qualitative aspect of the structure patterns populating the boundary layer is consistant with a realistic compressible turbulent boundary layer.

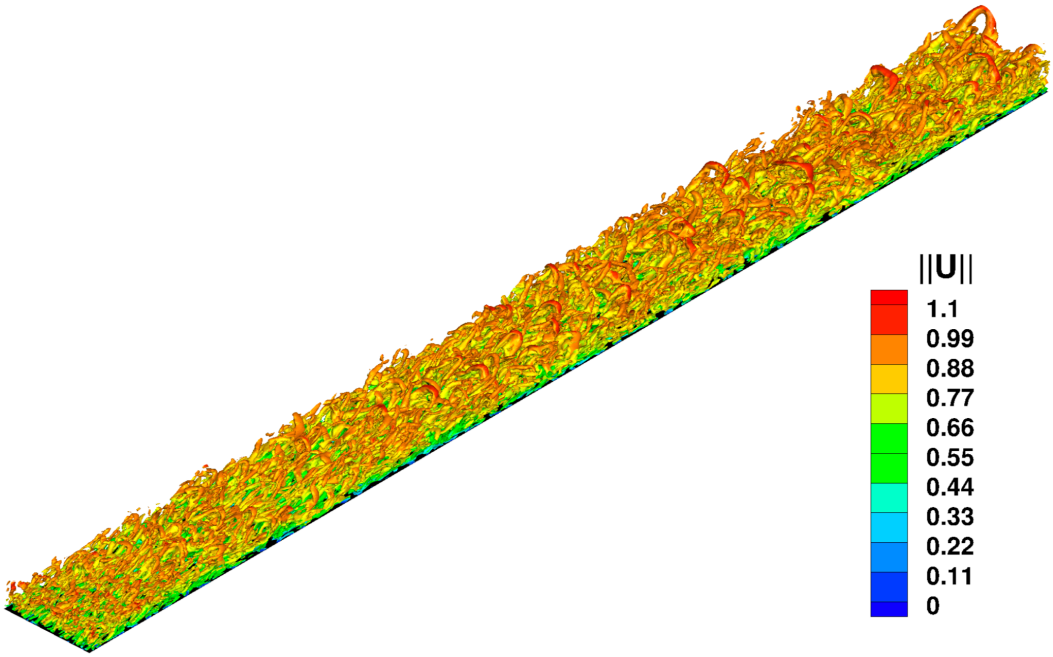

Fig. A.1. Q criterion ($\frac{\delta^2}{U_\infty^2}Q = 0.1$) colored by the velocity magnitude between $x = 0$ and $x = 40\delta$.

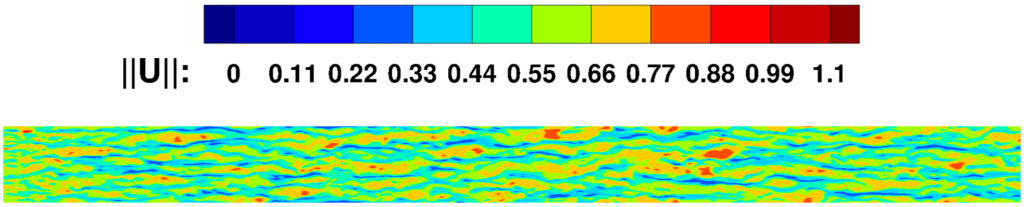

Fig. A.2. Isocontours of the velocity magnitude in a (x, z) plane at $y^+ \simeq 15$ above the wall, between $x = 0$ and $x = 40\delta$.

The mean skin friction coefficient, averaged in both time and in the spanwise direction is plotted along the flat plate in figure A.3. The adjustment distance needed to recover the right value of the skin friction coefficient is approximately $\Delta \sim 10\delta - 15\delta$. This adjustment distance appears to be very small compared to the one obtained in [41], in which a steady counterflow actuator with properties based on a dielectric barrier discharge is employed to trip an incoming laminar boundary layer. The simulation of [41] was performed using 2 meshes: a coarse mesh ($\Delta x^+ = 23.5$, $\Delta y_w^+ = 0.4$, $\Delta z^+ = 8.9$ at $x = 65\delta$) and a finer mesh ($\Delta x^+ = 16.4$, $\Delta y_w^+ = 0.4$, $\Delta z^+ = 6.1$ at $x = 65\delta$). Our mesh is comparable to the finest mesh of [41]. The adaptation distance obtained using the implemented SEM compares also well with respect to other tur-

bulent inflow conditions. For instance, the digital filter-based approach used in SWTBLI by [9] needed an adaptation of about 20δ to recover good skin friction coefficient. Moreover, the mean skin friction coefficient obtained here is in accordance with the values obtained in other studies for comparable compressible turbulent boundary layer simulations [10,8,9].

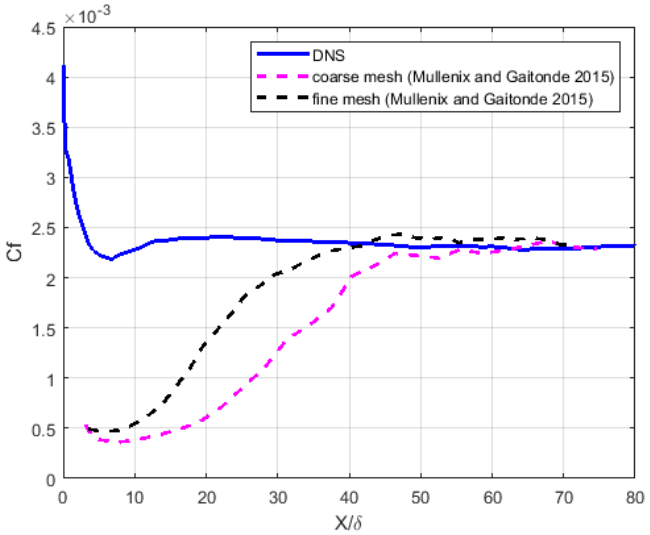

Fig. A.3. Time mean skin friction coefficient (C_f) averaged in the spanwise direction along the flat plate (x/δ).

Figure A.4 shows the Van Driest velocity profile and the Reynolds stress profiles with respect to y^+ obtained at $x = 20\delta$. The profiles correspond to time mean values averaged in the spanwise direction. The velocity is transformed into an equivalent non-dimensional incompressible velocity using the Van Driest transformation [50]:

$$u^+_{VD} = \frac{U_\infty}{u_\tau}\frac{1}{A}[\arcsin(\frac{2A^2u - B}{\sqrt{(4A^2 + B^2)}}) + \arcsin(\frac{B}{\sqrt{(4A^2 + B^2)}})] \tag{A.14}$$

where

$$\begin{aligned} A^2 &= \tfrac{\gamma-1}{2} M^2_\infty \tfrac{T_\infty}{T_w} \\ B &= (1 + \tfrac{\gamma-1}{2} M^2_\infty)\tfrac{T_\infty}{T_w} - 1 \end{aligned} \tag{A.15}$$

The Reynolds stresses are density-scaled and normalized by the friction velocity as follows:

$$R_{ij} = \frac{\overline{\rho}\overline{u'_i u'_j}}{\overline{\rho}_w \overline{u}^2_\tau} \tag{A.16}$$

The Van Driest velocity profile obtained at $x = 20\delta$ corresponds to a turbulent profile with a linear evolution close to the wall, followed by a logarithmic law evolution in the inertial region with the right parameters ($300 \leqslant y^+ \leqslant 2000$)

and by a wake region for ($2000 \leqslant y^+$). The Reynolds stress profiles obtained at $x = 20\delta$ are also realistic profiles for a compressible turbulent boundary layer. In particular, the value and the location of the peak of streamwise normal stress fall within the range reported in other studies ([41]: $R_{11} = 9.24$ at $y^+ = 18.11$, [9]: $R_{11} = 8.75$ at $y^+ \simeq 18$, [55]: $R_{11} = 8$ at $y^+ \simeq 15$). Moreover, the profile of R_{12} recovers a plateau-like evolution in the inertial range that is around -1 which is in accordance with the boundary layer theory.

An adaption length of about 20δ is then enough to recover realistic values of the skin friction coefficient, a realistic streamwise velocity profile and Reynolds stress profiles.

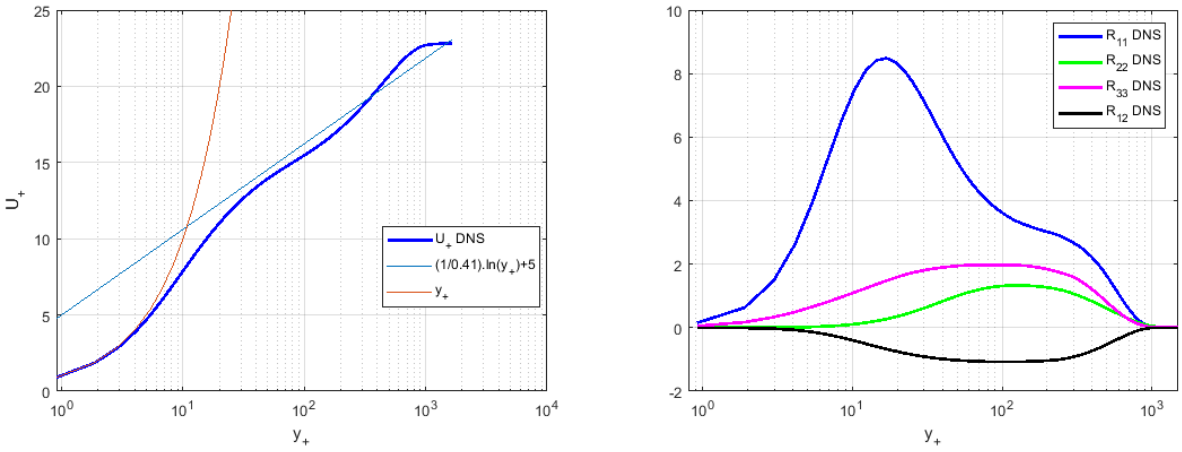

Fig. A.4. Left: Velocity profiles in the Van Driest transformed coordinates for $x = 20\delta$. Right: Density-scaled Reynolds stresses for $x = 20\delta$.

A line of probes oriented in the spanwise direction with one probe in each mesh cell has been placed at $x = 10\delta$ and $y_+ = 113$ ($y/\delta \simeq 0.28$). The spanwise autocorrelations of ρ, u, v, w and p fluctuations are plotted in figure A.5-left. These autocorrelations are computed as follows (see [55]):

$$C_{\alpha\alpha}(r_z = k_r \Delta z) = \sum_{k=1}^{N_z - 1} \overline{\alpha'_k \alpha'_{k+k_r}}, \quad k_r = 0, 1..., N_z - 1 \tag{A.17}$$

where N_z is the number of grid points in the $\mathbf{z}$ direction and α is the variable considered.

v fluctuations have a much wider correlation than u, which is larger than w, which has the narrowest correlation. The density fluctuation correlations are slightly wider than the correlations of v, whereas the pressure is the widest correlation. Figure A.5-left confirms that the spanwise extent of the domain is large enough such that the fluctuations at the midway point are de-correlated with fluctuations near the boundaries. The Taylor scales can be

calculated from the autocorrelation profiles. Regarding the longitudinal velocity (u), the Taylor microscale is $\lambda = 7.10^{-4}m$ and the Taylor macroscale is $\Lambda = 1.05.10^{-3}m$. These values then give following ratios with grid spacings: $\lambda/\Delta x \simeq 1.7$ and $\lambda/\Delta z \simeq 4.95$. The grid spacing in the longitudinal and spanwise direction is then significantly smaller than the characteristic scale of the smaller turbulent structures. Moreover $\Lambda/Lz \simeq 6.6.10^{-2}$ (with Lz the spanwise extent of the computational domain) indicating that the largest turbulent structures present in the domain are significantly small with respect to the spanwise extent of the computational domain.

The 1-D power spectra of ρ, u, v, w and p in the spanwise direction at $x = 10\delta$ and $y_+ = 113$ are plotted in figure A.5-right. The energy of these variables versus the spanwise wave number are computed as follows (see [55]):

$$E_{\alpha\alpha}(k_z = \frac{n}{(N_z-1)}\frac{1}{\Delta z}) = 1+2\sum_{k_r=1}^{(N_z-1)/2} C_{\alpha\alpha}(k_r\Delta z)cos(\frac{2\pi n k_r}{N_z-1}), \quad n = 0, 1..., (N_z-1)/2 \tag{A.18}$$

These spectra show that no spurious energetic length scale is introduced due to the SEM in the boundary layer. This point is crucial to judge the quality of the method. The spectral content is realistic for a compressible turbulent boundary layer. Moreover, for the velocity components, there is a significant region where the spectra follow a $k^{-5/3}$ profile.

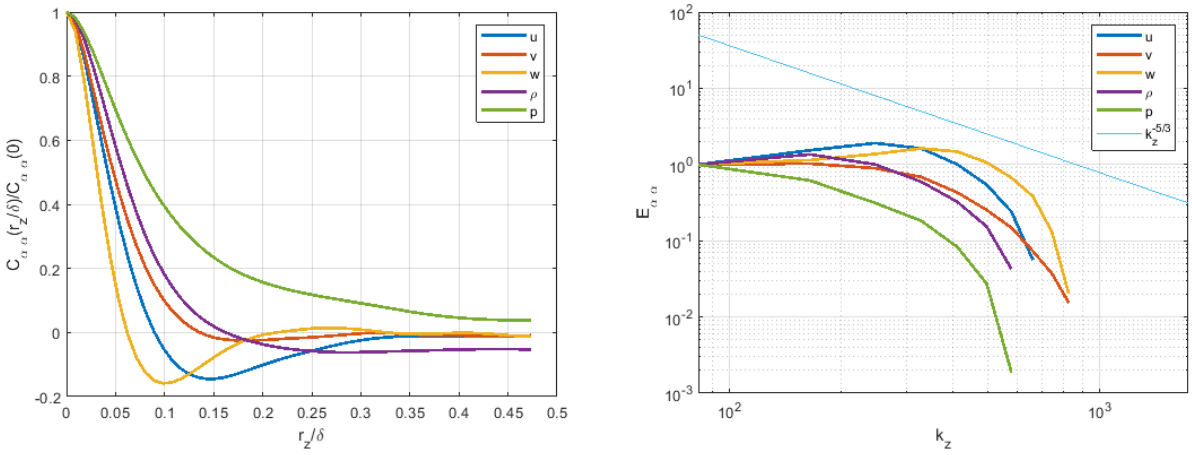

Fig. A.5. Left: Spanwise autocorrelations of the fluctuations at $x = 10\delta$ and $y_+ = 113$ ($y/\delta \simeq 0.28$). Right: Power spectra in the spanwise direction at $x = 10\delta$ and $y_+ = 113$ ($y/\delta \simeq 0.28$).

Moreover, as mentioned in the core of this paper, both the streamwise velocity and the Reynolds stress profiles are in very good agreement with reference values obtained from [41] (see Fig. 19). Especially, trends generally admitted for the Reynolds stress profiles in the inertial region [42] are very well recov-

ered, mainly for R_{33} that better fits the trend than the Mullenix and Gaitonde results [41], and for R_{12} that recovers a plateau evolution at a value -1 that is fully consistent with the energetic equilibrium assumption. The profile of the mean temperature (T) is also in good agreement with [41] showing the ability of the numerical approach (numerical scheme + fine mesh + SEM) to accurately compute thermodynamic fields.

A.2.1 Influence of the accuracy order of approximation of the diffusive fluxes.

In section 4.3, the influence of the accuracy order of approximation of the diffusive fluxes have been studied for the 3D Taylor-Green vortex at $Re = 1600$. It has been shown that using approximations of order higher than the 2^{nd}-order for the diffusive fluxes is not relevant for such unbounded high Reynolds number configurations. In order to check whether this conclusion also holds for a wall-bounded flow, the simulation of the same boundary layer on the same mesh has been performed using a 4^{th}-order centered finite difference approximation for the diffusive fluxes.

The results obtained with 2^{nd} or a 4^{th}-order approximations for the diffusive fluxes are compared for several quantities. The time mean skin friction coefficient, averaged in the spanwise direction is plotted along the flat plate in figure A.6. Figure A.7 shows the Van Driest velocity profile and the Reynolds stress profiles with respect to y^+. The temperature profile is shown in figure A.8. For all of these quantities, no or at least very little discrepancies are observed between results. It confirms the conclusion of section 4.3. Using approximations of order higher than the 2^{nd}-order for the diffusive fluxes is not relevant also for the simulation of such turbulent compressible boundary layer.

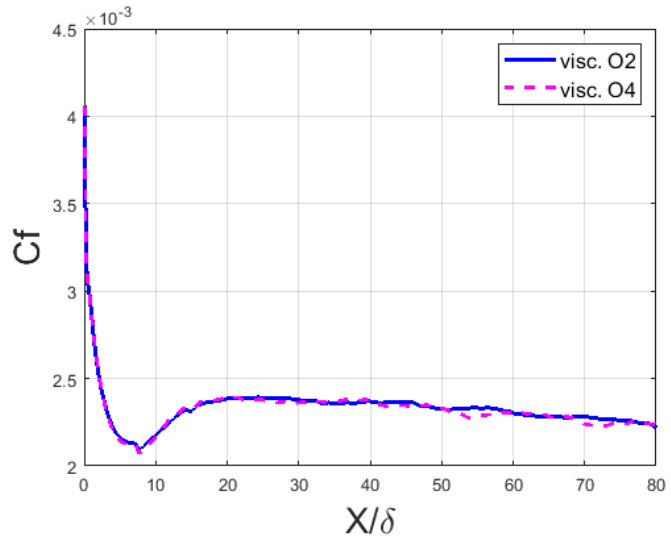

Fig. A.6. Comparison between the results obtained with a 2^{nd} order and a 4^{th} order discretization of the diffusive fluxes. Time mean skin friction coefficient (C_f) averaged in the spanwise direction along the flat plate (x/δ).

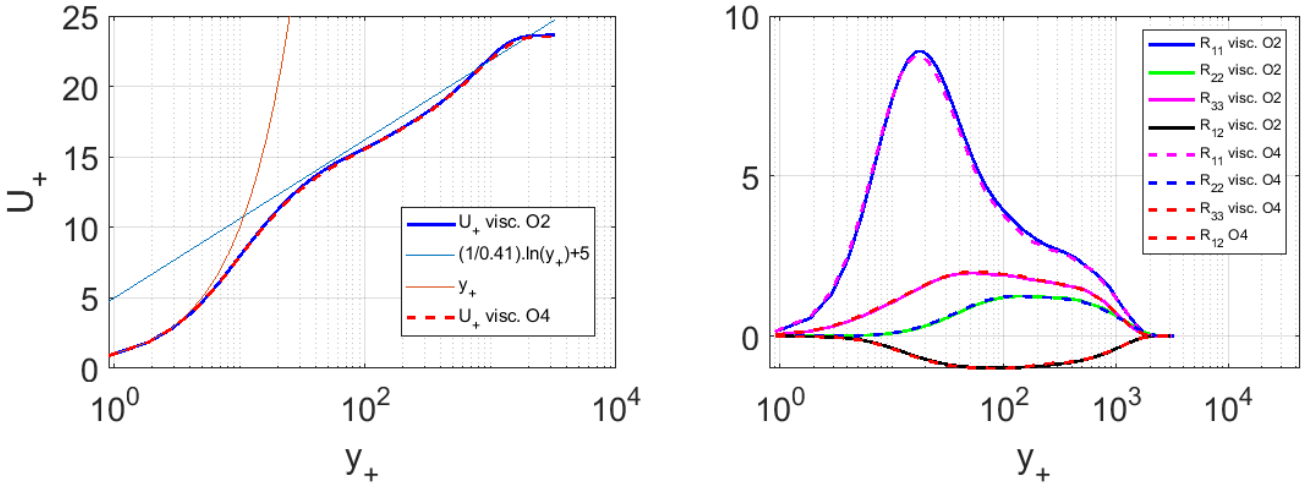

Fig. A.7. Comparison between the results obtained with a 2^{nd} order and a 4^{th} order discretization of the diffusive fluxes for $Re_\theta \simeq 3500$ and $x/\delta = 62.5$. Left: Velocity profiles in the Van Driest transformed coordinates. Right: Density-scaled Reynolds stresses. Right: Density-scaled Reynolds stresses.

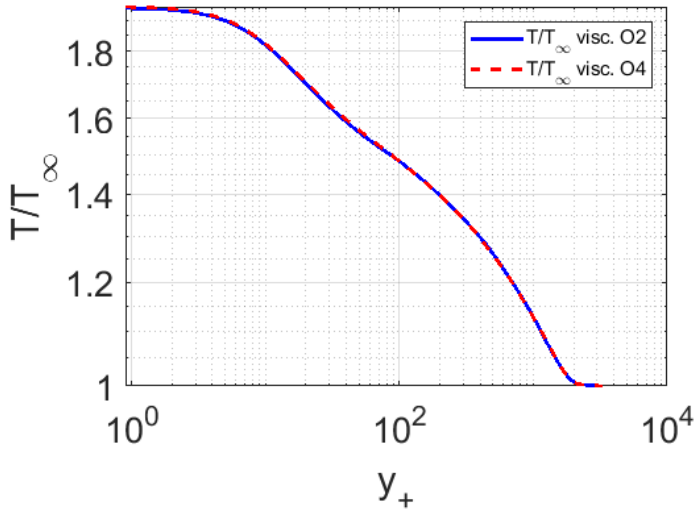

Fig. A.8. Comparison between the results obtained with a 2^{nd} order and a 4^{th} order discretization of the diffusive fluxes. Temperature profile.

B Some characteristic quantities of the boundary layer

We here recall the definitions of some characteristic quantities of the boundary layer:

- the boundary layer momentum thickness $\theta = \int_0^\infty \frac{\rho u}{\rho_\infty U_\infty}(1 - \frac{u}{U_\infty})dy$
- the displacement thickness $\delta^* = \int_0^\infty 1 - \frac{\rho u}{\rho_\infty U_\infty} dy$
- the shape factor $H = \frac{\delta^*}{\theta}$
- the friction velocity $u_\tau = \sqrt{\frac{\tau_w}{\rho_w}}$, where τ is the shear stress and the subscript w refers to the value of variables evaluated at the wall

C Prescribed mean velocity profile at the inlet of the domain

The mean velocity profile of the boundary layer at the inlet of the domain is prescribed using the analytical approximation introduced in [49]. Only the longitudinal component $\overline{u}_1$ is not null. It is build from prescribed values of the free stream velocity U_∞, the skin friction coefficient C_f, the boundary layer

momentum thickness θ and the shape factor H:

$$\overline{u}_1(y) = u_\tau \frac{1}{0.09}\text{atan}(0.09y^+) + (\mid \frac{C_f}{2} \mid^{-1/2} - \frac{\pi}{0.18})(\tanh(a(\frac{y}{\theta})^b))^{1/2}, \quad \text{(C.1)}$$

where $y^+ = \dfrac{u_\tau y}{\nu_w}$ is the vertical coordinate in wall units characterizing the viscous sublayer and:

$$u_\tau = U_\infty \mid \frac{C_f}{2} \mid^{1/2}$$

$$a = (\text{arctanh}(g^2(2)))/2^b$$

$$b = (\ln(\frac{\text{arctanh}(g^2(2))}{\text{arctanh}(g^2(5))}))/\ln(\frac{2}{5}),$$

$$g(2) = (\frac{U}{U_\infty}(2) - \frac{1}{0.09}(\frac{\mid C_f \mid}{2})^{1/2}\text{atan}(0.18Re_\theta(\frac{\mid C_f \mid}{2})^{1/2}))/(1 - \frac{\pi}{0.18}(\frac{\mid C_f \mid}{2})^{1/2}),$$

$$g(5) = (\frac{U}{U_\infty}(5) - \frac{1}{0.09}(\frac{\mid C_f \mid}{2})^{1/2}\text{atan}(0.45Re_\theta(\frac{\mid C_f \mid}{2})^{1/2}))/(1 - \frac{\pi}{0.18}(\frac{\mid C_f \mid}{2})^{1/2}),$$

$$\frac{U}{U_\infty}(2) = (\text{arctanh}(\frac{8.5 - H}{7.5}) - 0.364)/1.95,$$

$$\frac{U}{U_\infty}(5) = 0.155 + 0.795\cosh(0.51(H - 1.95)), \quad \text{(C.2)}$$

Even if the formulation $u_\tau = U_\infty \mid \dfrac{C_f}{2} \mid^{1/2}$ holds only for an incompressible boundary layer, we use this relationship to prescribe the mean velocity profile at the inlet of the simulation domain without knowing ρ_w.

D Generation of the random signal $\widetilde{u}_j(y, z, t)$

To generate the random signal $\widetilde{u}_j(y, z, t)$, we follow the approach introduced in [25], where the original SEM has been extended to account for the inhomogeneity of scales in the direction normal to the wall for boundary layer computations. Using this approach, the inlet plane is split into Þ zones in

which the random signal has different scales.

The random signal $\widetilde{u}_j(y,z,t)$ is then computed as a sum over the Þ zones,

$$\widetilde{u}_j = \sum_{p=1}^{\text{Þ}} \widetilde{v}_{jp}, \tag{D.1}$$

where $\widetilde{v}_{jp}$ are random velocity signals that have compact support on the p^{th} zone and are referred to as modes.

Each mode is the superposition of $N(p)$ structures. Each structure of the mode have a random time of appearance t_k and a random location of its center (y_k, z_k) in the p^{th} mode's zone, namely in $[y_p^{low}; y_p^{up}][0; L_z]$ where $y_p^{up} - y_p^{low}$ defines the wall normal extent of the p^{th} zone and L_z is the width of the inlet plane. The number of structures per mode $N(p)$ is chosen so that the p^{th} zone of the inlet plane is statistically covered by structures:

$$N(p) = \frac{S_p}{S_s}, \tag{D.2}$$

where S_p is the surface of the p^{th} zone ($S_p = L_z(y_p^{up} - y_p^{low})$) and S_s is the surface of a structure of the p^{th} mode projected onto the inlet plane ($S_S = 4 l_p^y l_p^z$).

Each mode is characterized by the length scales in each direction that are assigned to the structures and that are noted l_p^x, l_p^y and l_p^z. Using the Taylor's frozen turbulence hypothesis, l_p^x is related to a time scale of the structure l_p^t that characterizes the time necessary for a structure to fully pass through the inlet plane:

$$l_p^t = \frac{l_p^x}{c_p}, \tag{D.3}$$

where c_p is the convection velocity of structures that depends on the mode.

The shape of structures is characterized by shape functions in each direction g_{jp} depending on the mode. These shape functions depend on time and space coordinates through a product of mono-dimentional functions $\Xi(\widetilde{t})$, $\Phi(\widetilde{y})$ and $\Psi(\widetilde{z})$ where $\widetilde{t} = \dfrac{t - t_k - l_p^t}{l_p^t}$, $\widetilde{y} = \dfrac{y - y_k}{l_p^y}$ and $\widetilde{z} = \dfrac{z - z_k}{l_p^z}$ are the reduced variables for time, wall-normal and spanwise directions respectively. The random signal writes finally:

$$\begin{aligned} \widetilde{u}_j &= \textstyle\sum_{p=1}^{P} \widetilde{v}_{jp} = \sum_{p=1}^{P} \frac{1}{\sqrt{N(p)}} \sum_{k=1}^{N(p)} \epsilon_k \Xi_{jp}(\widetilde{t}) \Phi_{jp}(\widetilde{y}) \Psi_{jp}(\widetilde{z}), \\ &= \textstyle\sum_{p=1}^{P} \frac{1}{\sqrt{N(p)}} \sum_{k=1}^{N(p)} \epsilon_k g_{jp}(\widetilde{t}, \widetilde{y}, \widetilde{z}), \end{aligned} \tag{D.4}$$

where ϵ_k is a random sign (i.e. ± 1) assigned to each structure in order to decorrelate the components and to match the zero covariance condition ($\widetilde{u_i}\widetilde{u_j} \mid_{i \neq j} = \delta_{ij}$).

Using the formulation D.4, each structure is convected through the inlet plane. When $(t - t_k - l_p^t)/l_p^t = 1$, the structure k has completely passed through the inlet plane and a new structure is built with a random location (y_k, z_k) and a new random time of appearance chosen in $[t; t + l_p^t]$.

In order to prescribe a random signal with unit variance, the shape functions are normalized as follows:

$$\frac{1}{2^3} \int_{[-1;1]^3} [g_{jp}]^2(\tilde{t}, \tilde{y}, \tilde{z})]^2 d\tilde{t} d\tilde{y} d\tilde{z} = 1, \tag{D.5}$$

with $[-1; 1]$ the support of the shape functions that depend on normalized variables.

The inlet boundary conditions are completely defined when the scales l_p^t, l_p^y and l_p^z are chosen and when the functions $\Xi(\widetilde{t})$, $\Phi(\widetilde{y})$ and $\Psi(\widetilde{z})$ are defined for each mode. These scales and functions are defined in order to mimic the shapes and scales of the turbulent structures in a boundary layer. This approach is also used in [56] and the parameters and shape functions used in our implementation are extracted from [56]. The inlet plane is divided into 4 zones, the 1^{st} zone being the closest to the wall and the 4^{th} zone being the farthest from the wall. The low and up limits of the 4 zones expressed in wall units are given in table D.2. Close to the wall (1^{st} mode), structures injected in the domain have a long and a thin streamwise structure as in an real boundary layer. The 2^{nd} mode just above the first one, corresponding to the logarithmic layer, is populated by shorter and thicker structures reproducing the shape of hairpin vortices characteristic of the logarithmic layer. The rest of the boundary layer (3^{rd} and 4^{th} modes), are filled with Gaussian isotropic structures.

The shape functions corresponding to each mode are given in the table D.1 where:

$$H(\xi) = \frac{1 - cos(2\pi\xi)}{2\pi\xi\sqrt{0.214}} \tag{D.6}$$

and

$$G(\xi) = A(\sigma) e^{-\frac{\xi^2}{2\sigma^2}} \tag{D.7}$$

with $A(\sigma) = \dfrac{1}{\sigma \frac{\sqrt{\pi}}{2}} \mathrm{erf}(\dfrac{1}{\sigma})$ and $\sigma = \frac{1}{3}$.

Table D.1
Analytical expression of the shape functions. ϵ_1, ϵ_2 and ϵ_3 are random signs (i.e. ± 1).

	g_{1p}	g_{2p}	g_{3p}
p=1,2	$G(\tilde{t})G(\tilde{y})H(\tilde{z})$	$-G(\tilde{t})G(\tilde{y})H(\tilde{z})$	$G(\tilde{t})H(\tilde{y})G(\tilde{z})$
p=3,4	$\epsilon_1 G(\tilde{t})G(\tilde{y})G(\tilde{z})$	$\epsilon_2 G(\tilde{t})G(\tilde{y})G(\tilde{z})$	$\epsilon_3 G(\tilde{t})G(\tilde{y})G(\tilde{z})$

The length scales and the convection velocity of turbulent structures associated with each mode, expressed in wall units are given in table D.2.

Table D.2
Low and up limits, length scales and convection velocity of turbulent structures associated with each mode, expressed in wall units.

	$(y_p^{low})^+$	$(y_p^{up})^+$	$(l_p^y)^+$	$(l_p^x)^+$	$(l_p^z)^+$	c_p^+
p=1	20	40	20	100	30	15
p=2	40	0.188 δ	40	80	40	18
	(y_p^{low})	(y_p^{up})	(l_p^y)	(l_p^x)	(l_p^z)	c_p
p=3	0.188 δ	0.72 δ	0.125 δ	0.125 δ	0.125 δ	0.76 U_∞
p=4	0.4 δ	1.7 δ	0.227 δ	0.227 δ	0.227 δ	0.76 U_∞

References

[1] V. Daru, C. Tenaud, Evaluation of tvd high resolution schemes for unsteady viscous shocked flows, Computers and Fluids 30 (Issue 1) (2001) 89–113.

[2] V. Daru, C. Tenaud, High order one-step monotonicity-preserving schemes for unsteady compressible flow calculations, Journal of Computational Physics 193 (2) (2004) 563 – 594.

[3] Z. Wang, K. Fidkowski, R. Abgrall, F. Bassi, D. Caraeni, A. Cary, H. Deconinck, R. Hartmann, K. Hillewaert, H. Huynh, N. Kroll, G. May, P.-O. Persson, B. van Leer, M. Visbal, High-order cfd methods: current status and perspective, International Journal for Numerical Methods in Fluids 72 (8) (2013) 811–845.

[4] J. Delery, Some physical aspects of shock wave/boundary layer interactions, Shock Waves 19 (6) (2009) 453–468.

[5] D. V. Gaitonde, Progress in shock wave/boundary layer interactions, Progress in Aerospace Sciences 72 (2015) 80–99, celebrating 60 Years of the Air Force Office of Scientific Research (AFOSR): A Review of Hypersonic Aerothermodynamics.

[6] S. Lee, S. K. Lele, P. Moin, Direct numerical simulation of isotropic turbulence interacting with a weak shock wave., Journal of Fluid Mechanics 251 (1993) 533–562.

[7] S. Pirozzoli, Numerical methods for high-speed flows, Annual Review of Fluid Mechanics 43 (1) (2011) 163–194.

[8] S. Pirozzoli, F. Grasso, Direct numerical simulation of impinging shock wave/turbulent boundary layer interaction at M=2.25, Physics of Fluids 18 (6) (2006) 065113.

[9] E. Touber, N. D. Sandham, Large-eddy simulation of low-frequency unsteadiness in a turbulent shock-induced separation bubble, Theoretical and computational fluid dynamics 23 (2) (2009) 79–107.

[10] G. Aubard, X. Gloerfelt, J.-C. Robinet, Large-eddy simulation of broadband unsteadiness in a shock/boundary-layer interaction, AIAA Journal 51 (2013) 2395–2409.

[11] A. Hadjadj, Large-eddy simulation of shock/boundary-layer interaction, AIAA Journal 50 (12) (2012) 2919–2927.

[12] S. Priebe, J. H. Tu, C. W. Rowley, M. P. Martín, Low-frequency dynamics in a shock-induced separated flow, Journal of Fluid Mechanics 807 (2016) 441–477.

[13] S. Del Pino, H. Jourdren, Arbitrary high-order schemes for the linear advection and wave equations: application to hydrodynamics and aeroacoustics, Comptes Rendus Mathematique 342 (Issue 6) (2006) 441–446.

[14] A. Harten, B. Engquist, S. Osher, S. Chakravarthy, Uniformly high order essentially non-oscillatory schemes, iii, Journal of Computational Physics 71 (1987) 231–303.

[15] G. Strang, Accurate partial difference methods. i. linear cauchy problems, Arch. Ration. Mech. Anal. 12 (1963) 392–402.

[16] G. Strang, On the construction and comparison of difference schemes, SIAM J. Numer. Anal. 5 (1968) 506–517.

[17] R. J. Leveque, Numerical Methods for Conservation Laws, 2nd Edition, Springer, 1992.

[18] A. Harten, High Resolution Schemes for Hyperbolic Conservation Laws, Journal of Computational Physics 49 (3) (1983) 357–393.

[19] A. Suresh, H. Huynh, Accurate monotonicity-preserving scheme with runge-kutta time stepping, Journal of Computational Physics 136 (1) (1997) 83–99.

[20] X.-D. Liu, S. Osher, T. Chan, Weighted essentially non-oscillatory schemes, Journal of computational physics 115 (1) (1994) 200–212.

[21] D. S. Balsara, S. C.-W., Monotonicity preserving weighted essentially non-oscillatory schemes with increasingly high order of accuracy, Journal of computational physics 160 (Issue 2) (2000) 405–452.

[22] V. Daru, C. Tenaud, Numerical simulation of the viscous shock tube problem by using a high resolution monotonicity-preserving scheme, Computers & Fluids 38 (2009) 664–676.

[23] O. Tenaud, C.; Roussel, L. Bentaleb, Unsteady compressible flow computations using an adaptive multiresolution technique coupled with a high-order one-step shock-capturing scheme, Computers and Fluids 120 (2015) 111–125.

[24] N. Jarrin, S. Benhamadouche, D. Laurence, R. Prosser, A synthetic-eddy-method for generating inflow conditions for large-eddy simulation, International Journal of Heat and Fluid Flow 27 (4) (2006) 585–593.

[25] M. Pamiès, P.-É. Weiss, E. Garnier, S. Deck, Generation of synthetic turbulent inflow data for large eddy simulation of spatially evolving wall-bounded flows, Physics of fluids 21 (2009) 045103.

[26] V. Daru, X. Gloerfelt, Aeroacoustic computations using a high-order shock-capturing scheme, AIAA Journal 45 (10) (2007) 2474–2486.

[27] M. Brachet, D. I. Meiron, S. A. Orszag, B. G. Nickel, R. H. Morgf, u. Frish, Small-scale structure of the Taylor-Green vortex, Journal of fluid mechanics 130 (23) (2006) 411–452.

[28] S. K. Lele, Compact finite difference schemes with spectral-like resolution, Journal of Computational Physics 103 (1) (1992) 16–42.

[29] HiOCFD4 Committee, 4th international workshop on high-order cfd methods, [https://how4.cenaero.be] (2016).

[30] G. Degrez, C. H. Boccadoro, J. F. Wendt, The interaction of an oblique shock wave with a laminar boundary layer revisited. An experimental and numerical study, Journal of fluid mechanics 177 (13) (1987) 247–263.

[31] R. Blanchard, F. Renac, Baseline test case summaries. case bl2: Shock wave / laminar boundary layer interaction, [https://how4.cenaero.be] (2016).

[32] K. Thompson, Time Dependent Boundary Conditions for Hyperbolic Systems, Journal of computational physics 68 (1) (1987) 1–24.

[33] A. Gross, H. F. Fasel, Numerical Investigation of Shock Boundary-Layer Interactions, 2016, pp. 1–23.

[34] E. Touber, N. Sandham, Oblique shock impinging on a turbulent boundary layer: Low-frequency mechanisms., 2008. doi:10.2514/6.2008-4170.

[35] H. Babinsky, J. K. Harvey, Shock wave-boundary-layer interactions, Vol. 32, Cambridge University Press, 2011.

[36] R. Cherry, N. J.; Hillier, M. E. M. P. Latour, Unsteady measurements in a separated and reattaching flow, Journal of Fluid Mechanics 144 (1984) 13–46. doi:10.1017/S002211208400149X.

[37] M. Kiya, K. Sasaki, Structure of large-scale vortices and unsteady reverse flow in the reattaching zone of a turbulent separation bubble, Journal of Fluid Mechanics 154 (1985) 463–491. doi:10.1017/S0022112085001628.

[38] W. Wu, C. Meneveau, M. R., Spatio-temporal dynamics of turbulent separation bubbles, Journal of Fluid Mechanics 883 (2020) A45–1–A45–37.

[39] P. Dupont, S. Piponniau, A. Sidorenko, J. François Debiève, Investigation of an oblique shock reflection with separation by piv measurements, in: Proceedings of the 45th AIAA Aerospace Sciences Meeting and Exhibit, 2007.

[40] S. Piponniau, J. P. Dussauge, J. F. Debiève, P. Dupont, A simple model for low-frequency unsteadiness in shock-induced separation, Journal of Fluid Mechanics 629 (2009) 87–108.

[41] N. J. Mullenix, D. V. Gaitonde, M. R. Visbal, Spatially developing supersonic turbulent boundary layer with a body-force-based method, AIAA journal 51 (8) (2013) 1805–1819.

[42] A. E. Perry, J. D. Li, Experimental support for the attached-eddy hypothesis in zero-pressure-gradient turbulent boundary layers., Journal of Fluid Mechanics 218 (1990) 405–438.

[43] M. C. Adler, D. V. Gaitonde, Dynamic linear response of a shock/turbulent-boundary-layer interaction using constrained perturbations, Journal of Fluid Mechanics 840 (2018) 291–341.

[44] G. Aubard, Large Eddy Simulation of the low-frequency unsteadiness of a shock-wave turbulent boundary layer interaction on a flat plate, Theses, Arts et Métiers ParisTech (Jun. 2012).
URL https://pastel.archives-ouvertes.fr/pastel-00728991

[45] P. Sagaut, S. Deck, M. Terraco, Multiscale and Multiresolution Approaches in Turbulence., Imperial College Press, 2006.

[46] G. Tabor, M. Baba-Ahmadi, Inlet conditions for large eddy simulation: A review, Computers & Fluids 39 (2010) 553–567.

[47] N. Dhamankar, G. A Blaisdell, A. Lyrintzis, An overview of turbulent inflow boundary conditions for large eddy simulations, AIAA Journal 56 (35) (2017) 1–18.

[48] T. Lund, X. Wu, K. Squires, Generation of turbulent inflow data for spatially-developing boundary layer simulations, Journal of Computational Physics 140 (1998) 233–258.

[49] D. L. Whitfield, Analytical description of the complete turbulent boundary layer velocity profile, Final Report, Oct. 1976 - Mar. 1977 ARO, Inc., Arnold Air Force Station, TN.

[50] J. Cousteix, Aéerodynamique: Turbulence et Couche Limite, Cépaduès-editions, 1989.

[51] P. Bradshaw , D. H. Ferriss , N. P. Atwell , Calculation of boundary layer using the turbulent energy equation, Journal of Fluid Mechanics 28 (1967) 593 – 616.

[52] A. Townsend, The structure of turbulent shear flow, Cambridge Monogr. Mech. Appl. Math. 2.

[53] D. C. Wilcox, Turbulence modeling for CFD, 3rd Edition, DCW Industries, Inc., 2006.

[54] G. Aubard, X. Gloerfelt, J.-C. Robinet, Characterisation of synthetic turbulence methods for large-eddy simulation of supersonic boundary layers, in: Progress in Turbulence and Wind Energy IV, Springer Proceedings in Physics book series (SPPHY, volume 141), 2012, pp. 81–84.

[55] S. Pirozzoli, F. Grasso, T. Gatski, Direct numerical simulation and analysis of a spatially evolving supersonic turbulent boundary layer at M= 2.25, Physics of fluids 16 (3) (2004) 530–545.

[56] R. Laraufie, S. Deck, Assessment of reynolds stresses tensor reconstruction methods for synthetic turbulent inflow conditions. application to hybrid rans/les methods, International Journal of Heat and Fluid Flow 42 (2013) 68 – 78.